Title	Studies on Phenolic Compounds Decomposition through Liquid-phase Oxidation Using Ceria-Zirconia Based Catalysts
Author(s)	Supandi, Abdul Rohman
Citation	大阪大学, 2020, 博士論文
Version Type	VoR
URL	https://doi.org/10.18910/77484
rights	
Note	

Doctoral Dissertation

Studies on Phenolic Compounds Decomposition through Liquid-phase Oxidation Using Ceria-Zirconia Based Catalysts

(セリア-ジルコニア系触媒を用いた液相酸化による
フェノール類化合物の分解に関する研究)

ABDUL ROHMAN SUPANDI

July 2020

Department of Applied Chemistry

Graduate School of Engineering

Osaka University

Preface

The study of this thesis has been conducted under the supervision of Professor Dr. Nobuhito Imanaka at Department of Applied Chemistry, Graduate School of Engineering, Osaka University.

The object of this thesis is to develop novel environmental catalysts for the decomposition of phenolic compounds under moderate condition.

The author wishes that the findings and the knowledge obtained in this work will provide useful suggestions and information for further development and design of novel environmental catalysts and that the materials would contribute to more practical applications.

Abdul Rohman Supandi

Department of Applied Chemistry
Graduate School of Engineering
Osaka University
2-1 Yamadaoka, Suita,
Osaka 565-0871,
Japan

July, 2020

Contents

Chapter 1

Liquid-phase Oxidation of Phenolic Compounds Using Pt/CeO_2-ZrO_2-SnO_2 Supported on SBA-16

Chapter 2

Liquid-phase Oxidation of Phenol Using Pt/CeO_2-ZrO_2-SnO_2 Supported on ZrO_2/SBA-16

Chapter 3

Liquid-phase Oxidation of Phenol Using Pt/CeO_2-ZrO_2-Bi_2O_3 Supported on Size-controlled ZrO_2

General Introduction

Over the past several decades, the rapid and continuous development of the industrial sector has caused an increase in the number of hazardous pollutants released due to the excess of raw materials. Phenolic compounds, such as phenol and cresols, are well-known pollutants, frequently found in the industrial wastewater stream because they have been widely used in many kinds of manufacturing processes; e.g., phenol resins, acetylsalicylic acid, and pesticide [1-3]. As the direct application, phenolic compounds have been used in medical, livestock-related, and industrial environments. However, phenolic compounds are highly toxic compounds for human health which may cause heart, kidney, liver, and nervous center system damages, and they are lethal to aquatic life even at low concentrations [2–5]. Moreover, several phenolic compounds (cresols, phenol, etc.) easily penetrate to the human skin and are also readily absorbed through oral ingestion [6,7]. Once they are incorporated into body system, they will be involved in the metabolism process and transform to various reactive intermediate forms resulting in their ability to exert toxic effects on humans [8]. Long-term exposure can also lead to irregular breathing, tremor, muscle weakness, coma, and respiratory arrest at lethal doses in humans [9,10]. Also, the trace amount of them in water causes the objectionable odor during the chlorination disinfection of drinking water [9,10]. In Japan, the effluent standard of the phenolic compounds have been regulated to be 5 $mg \cdot L^{-1}$ according to the Water Pollution Control Law, and some substances, e.g., phenol and cresols, have been monitored by the PRTR (Pollutant Release and Transfer Register) regulation. In addition, phenolic compounds are also enlisted as the priority pollutant to be concerned by USEPA (United States Environmental Protection Agency) and EU (European Union) [9,10]. Therefore, it is necessary to remove phenolic compounds from the wastewater stream as much as possible.

Currently, several wastewater treatment methods have been applied for the elimination of phenolic compounds, such as adsorption, coagulating sedimentation, and biological processes [9–16]. The adsorption process can easily remove phenolic compounds by pass through the adsorbent (e.g. active carbon, fly ash, etc.), while it has to be replaced with a new or regenerated one before reaching the adsorption capacity. Coagulating sedimentation is the technology in which phenolic compounds are sedimented by adding coagulant agent, although it requires the removal of the generated sediment and most of coagulants show low performance for phenolic compounds coagulation [13,14]. Biological treatment is commonly used due to its high efficiency for the phenolic compounds removal; however, it has also some disadvantages, e.g., long operating periods, separation of the biological sludge, and the control of dissolved oxygen concentration, pH, and temperature for microorganisms [15–17]. On the other hand, liquid-phase oxidation using strong oxidizing agents [18,19], Fenton (-like) reagents [18-26], UV irradiation [27,28], and ultrasonic irradiation [28,29] are regarded as an effective method for the phenolic compounds decomposition, as listed in Table G-1. In the case of the use of strong oxidizing agents such as H_2O_2, O_3, and peroxymonosulfate (PMS), the generated radical ($OH^\bullet$, $SO_4^{\bullet-}$, etc.) decomposes phenolic compounds [19-22]. Fenton reagent can be made by adding Fe^{2+} into the strong oxidizing agents, and the efficiency for the phenols decomposition is considerably improved because the Fe^{2+} ions facilitate the radical formation through such reactions, for example: $Fe^{2+} + H_2O_2 \rightarrow Fe^{3+} + OH^\bullet + OH^-$. Similar processes have been demonstrated by using Fe^{3+}, Cu^{2+}, Ni^{2+}, $NiFe_2O_4$, etc. instead of Fe^{2+}, which are referred to as Fenton-like reaction. Irradiation of UV or ultrasound can also accelerate the generation of radicals, resulting in the remarkable efficiency for the phenol removal. However, the continuous supply of hazardous oxidizing agent, light irradiation, and ultrasonic irradiation are indispensable for these methods.

Table G-1. Proposed liquid-phase oxidation of phenol using strong oxidizing agent, Fenton (-like) reagent, UV iiradiation, and ultrasonic irradiation

Experimental condition	Removal percentage (%)	Ref.
O_3, 20°C, 1 h, 0.1 MPa	40	[18]
PMS, 25°C, 6 h, 0.1 MPa	7	[19]
PMS + Carbon nanotube, 25°C, 2.5 h, 0.1 MPa	77	[20]
$H_2O_2 + Fe^{2+}$, 25°C, 2 h, 0.1 MPa	100	[21]
$H_2O_2 + Fe^{2+}$, 25°C, 0.5 h, 0.1 MPa	37	[22]
H_2O_2 + Fe/ZrO_2, 25°C, 6 h, 0.1 MPa	90	[23]
H_2O_2 + Fe-polyamidoxime, 25°C, 4 h, 0.1 MPa	71	[24]
H_2O_2 + Cu-polyamidoxime, 25°C, 4 h, 0.1 MPa	80	[24]
H_2O_2 + Zn-polyamidoxime, 25°C, 4 h, 0.1 MPa	77	[24]
H_2O_2 + Fe/sulfated ZrO_2, 25°C, 2 h, 0.1 MPa	100	[23]
$H_2O_2 + Cu^{2+}$, 20°C, 2 h, 0.1 MPa	92	[25]
$O_3 + NiFe_2O_4$, 20°C, 1 h, 0.1 MPa	55	[18]
PMS + Co/ZSM-5, 25°C, 6 h, 0.1 MPa	100	[19]
PMS + $ZnFe_2O_4$, 25°C, 3 h, 0.1 MPa	20	[26]
PMS + MnO_2, 25°C, 3 h, 0.1 MPa	100	[26]
O_3 + UV, room temperature, 50 min, 0.1 MPa	100	[27]
H_2O_2 + UV, room temperature, 50 min, 0.1 MPa	80	[27]
$H_2O_2 + Fe^{2+}$ + UV, room temperature, 0.5 h, 0.1 MPa	100	[28]
H_2O_2 + ultrasound, 25°C, 5 h, 0.1 MPa	25	[29]
O_3 + ultrasound, 25°C, 5 h, 0.1 MPa	37	[29]
H_2O_2 + ultrasound + ash, 25°C, 5 h, 0.1 MPa	84	[29]
O_3 + ultrasound + ash, 25°C, 5 h, 0.1 MPa	90	[29]
$H_2O_2 + Fe^{2+}$ + ultrasound, room temperature, 0.5 h, 0.1 MPa	70	[28]

Liquid-phase oxidation using oxygen gas molecule has been proposed as the simple and environmentally friendly method. However, this method required the elevated temperatures of 125–320°C and high pressures of 0.5–20 MPa for the effective removal because of insufficient reactivity and solubility of the oxygen molecule in the solution [30–32]. Catalytic liquid-phase oxidation method has been reported to decompose phenolic compounds without a supply of additives nor light and sonic irradiation, in which catalysts facilitate the oxidation of phenolic compounds using dissolved oxygen molecules. Although the high catalytic activity has been demonstrated for homogeneous catalysts [33,34], such as copper salts, they required post-process to separate the dissolved catalysts of toxic metal ion into the liquid-phase. The heterogeneous catalyst is more beneficial owing to serial reaction manners and its easy separation as well as recovering procedure. As the heterogeneous catalysts, typical metal oxides [4,35–43] and noble metal [44–48] based catalysts are summarized in Table G-2. Among the metal oxide systems, CuO, MoO_x, and CeO_2-TiO_2 based catalysts exhibited remarkable activities. However, they were deactivated owing to the leaching of the metal ion and the adsorption of intermediate products on the catalyst surface. In the case of noble metal (Ru, Pt, Pd) systems, while the Ru and Pd based catalysts showed the higher efficiency than that for Pt, the Ru and Pd systems were reported to generate the high amount of intermediate compounds, such as benzoquinone, which are harmful for human health and also may lead to the deactivation due to the adsorption on the catalyst surface. Therefore, the Pt based catalysts are considered to be appropriate ones from the viewpoints of the effective oxidation of phenol and the deactivation, while they required the severe conditions of 150–170°C and 1.7–5.05 MPa.

Table G-2. Summary of studies on liquid-phase oxidation of phenol using metal oxide and noble metal based catalysts

Catalyst	Removal percentage (%)	Reaction condition	Ref.
CeO_2	18	150°C, 3.0 MPa (air)	[4]
TiO_2	15	150°C, 3.0 MPa (air)	[4]
MnO_2	10	110°C, 0.5 MPa (O_2)	[35]
$CuO_x/\gamma\text{-}Al_2O_3$	100	150°C, 5.05 MPa (air)	[36,37]
$CuO_x/Ce_{0.65}Zr_{0.35}O_2$	100	150°C, 5.05 MPa (air)	[38]
CuO_x/MCM-41	98	150°C, 5.05 MPa (air)	[39]
$CuO_x/CeO_2/\gamma\text{-}Al_2O_3$	100	180°C, 1.5 MPa (O_2)	[40]
$NiO_x/\gamma\text{-}Al_2O_3$	~ 15	150°C, 5.05 MPa (air)	[36]
$NiO_x/Ce_{0.65}Zr_{0.35}O_2$	69	150°C, 5.05 MPa (air)	[38]
$CoO_x/\gamma\text{-}Al_2O_3$	~ 15	150°C, 5.05 MPa (air)	[36]
$CoO_x/Ce_{0.65}Zr_{0.35}O_2$	52	150°C, 5.05 MPa (air)	[38]
$FeO_x/\gamma\text{-}Al_2O_3$	~ 15	150°C, 5.05 MPa (air)	[36]
$FeO_x/Ce_{0.65}Zr_{0.35}O_2$	43	150°C, 5.05 MPa (air)	[38]
CeO_2/SiO_2	43	180°C, 1.5 MPa (O_2)	[41]
CeO_2/TiO_2	22	180°C, 1.5 MPa (O_2)	[41]
$MnO_x/\gamma\text{-}Al_2O_3$	50	150°C, 5.05 MPa (air)	[36]
$MnO_x/Ce_{0.65}Zr_{0.35}O_2$	92	150°C, 5.05 MPa (air)	[38]
$Ce_{0.80}Cu_{0.20}O_{2-\delta}$	100	150°C, 0.73 MPa (O_2)	[42]
$Cu_{0.10}Ce_{0.90}O_{2-\delta}$	97	150°C, 0.7 MPa (O_2)	[43]
$Ce_{0.40}Mn_{0.60}O_2$	90	110°C, 0.5 MPa (O_2)	[35]
$Ce_{0.33}Ti_{0.67}O_2$	50	150°C, 3.0 MPa (air)	[4]
$Ce_{0.50}Ti_{0.50}O_2$	90	150°C, 3.0 MPa (air)	[4]
Ru/ZrO_2	90	140°C, 2.0 MPa (air)	[44]
Ru/C	80	160°C, 2.0 MPa (O_2)	[45]
Ru/CeO_2	90	160°C, 2.0 MPa (O_2)	[45]
Ru/CeO_2	98	160°C, 2.0 MPa (O_2)	[46]
Ru/TiO_2	96	160°C, 2.0 MPa (O_2)	[46]
Pd/CeO_2	78	160°C, 2.0 MPa (O_2)	[45]
Pt/CeO_2	74	160°C, 2.0 MPa (O_2)	[45]
Pt/TiO_2	80	150°C, 1.7 MPa (air)	[47]
$Pt/\gamma\text{-}Al_2O_3$	70	170°C, 5.05 MPa (air)	[48]
$Pt/CeO_2/\gamma\text{-}Al_2O_3$	90	170°C, 5.05 MPa (air)	[48]

Here, to develop the heterogeneous catalyst with high efficiency in the liquid-phase, it is also important to use solid promoters which can effectively provide the oxygen species from their lattice to the active sites. Figure G-1 depicts the plausible process of oxygen supply from the promoter to activator for the decomposition of phenolic compounds in the liquid-phase. In general, since the phenolic compounds are oxidized by the adsorbed oxygen on the activator, oxygen species should be released toward the activator from inside the promoter lattice for the continuous reaction. To compensate the lattice oxygen in the promoter, the dissolved oxygen molecule is stored as oxide ion. The oxygen release and storage processes accompany the reduction and oxidation of the constituent metal cation in the promoter, respectively.

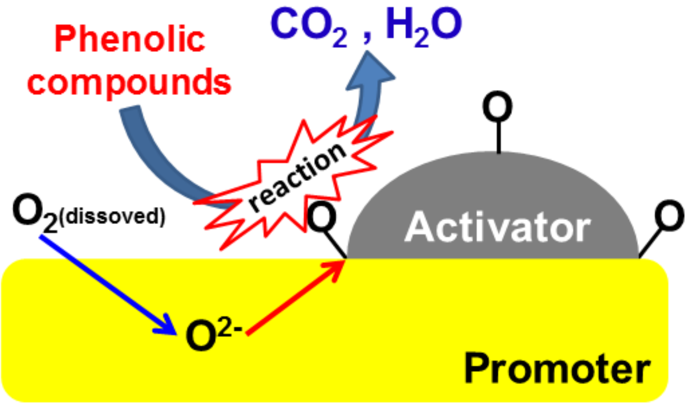

Figure G-1. Plausible process of oxygen supply on activator from promoter for the catalytic liquid-phase oxidation.

Ceria-zirconia solid solution (CeO_2-ZrO_2), which is widely used as a promoter for various catalysts, such as automotive exhaust catalyst, has been known to show the oxygen release and storage abilities owing to the reversible redox of Ce^{4+} and Ce^{3+} couple ions [49–51]. The ZrO_2 incorporation is known to be an important role for the high oxygen release and storage abilities of CeO_2-ZrO_2, caused by the improvement of the oxide ion mobility. For the catalytic liquid-phase oxidation of phenol, the CeO_2-ZrO_2 promoter has been recently paid attention to facilitate the oxygen supply from inside the lattice. Table G-3 shows the Pt/CeO_2-ZrO_2 based catalysts for the phenol oxidation [52,53]. Among them, the Pt/$Ce_{0.90}Zr_{0.10}O_2$ (Pt/CZ) catalyst was reported to show the highest activity, and 92% of phenol can be removed after the reaction for 3 h at 160°C and 2.0 MPa of pure oxygen pressure [52] (20 times higher than the atmospheric air pressure of 0.1 MPa). However, the condition was still severe for the practical application use.

Table G-3. Summary of studies on liquid-phase oxidation of phenol using Pt/CeO_2-ZrO_2 based catalysts

Catalyst	Removal percentage (%)	Reaction condition	Ref.
Pt/$Ce_{0.90}Zr_{0.10}O_2$	92	160°C, 2.0 MPa (O_2)	[52]
Pt/$Ce_{0.75}Zr_{0.25}O_2$	67	160°C, 2.0 MPa (O_2)	[52]
Pt/$Ce_{0.50}Zr_{0.50}O_2$	80	160°C, 2.0 MPa (O_2)	[52]
Pt/$Zr_{0.10}(Ce_{0.75}Pr_{0.25})_{0.90}O_2$	76	160°C, 2.0 MPa (O_2)	[53]

Based on the above mentioned backgrounds, this thesis aims to realize the phenolic compound decomposition through catalytic liquid-phase oxidation under moderate condition, i.e. low temperatures (below 100°C) and the atmospheric air pressure.

This thesis consists of the following three chapters.

In Chapter 1, mesoporous silica SBA-16, Santa Barbara Amorphous No. 16, having large surface area was used as a catalyst support to increase the number of active sites. In addition, CeO_2-ZrO_2-SnO_2 was selected as a promoter of a Pt catalyst, because the redox of $Sn^{4+/2+}$ has been reported to enhance the oxygen release and storage abilities of the CeO_2-ZrO_2 based solid [54]. Therefore, Pt/CeO_2-ZrO_2-SnO_2/SBA-16 was prepared, and the catalytic activities were investigated for phenol and *p*-cresol decomposition.

In Chapter 2, for further improvement of the catalytic activity, the study was focused on the acidity of the support, because it has been reported that the higher acidity of the material increased the dispersion of supported materials [55,56], expecting the enhancement of the oxygen release and storage abilities of the promoter by prohibiting the aggregation. Here, ZrO_2 was loaded on SBA-16 to increase the acidity of support, and the activities of Pt/CeO_2-ZrO_2-SnO_2/ZrO_2/SBA-16 catalysts were investigated for phenol decomposition.

In Chapter 3, the size-controlled ZrO_2 nanoparticles were used as supports, since the particle-size of the support is considered to affect the acidity, the oxygen release and storage abilities of the promoter, and the catalytic activity. In order to discuss strictly the ZrO_2 size effect on the catalytic activity, I selected CeO_2-ZrO_2-Bi_2O_3 having high oxygen release and storage abilities similar to CeO_2-ZrO_2-SnO_2 for the low temperature synthesis of catalyst. Thereby, the catalytic activities over Pt/CeO_2-ZrO_2-Bi_2O_3/ZrO_2 were investigated.

List of Publications

1. Liquid-phase Oxidation of Phenol in Facile Condition Using Pt/CeO_2-ZrO_2-SnO_2 Catalyst Supported on Mesoporous Silica SBA-16

   Abdul Rohman Supandi, Naoyoshi Nunotani, and Nobuhito Imanaka

   Journal of Environmental Chemical Engineering, 2017, *5*, 3999–4004.

2. Effective *p*-Cresol Removal through Catalytic Liquid-phase Oxidation under Moderate Conditions Using Pt/CeO_2-ZrO_2-SnO_2/SBA-16 as a Catalyst

   Abdul Rohman Supandi, Naoyoshi Nunotani, and Nobuhito Imanaka

   Journal of Asian Ceramic Societies, 2020, *8 (1)*, 116–122.

3. Complete Phenol Removal in Liquid-Phase under Moderate Condition over Pt/CeO_2-ZrO_2-SnO_2/ZrO_2/SBA-16 Catalysts

   Abdul Rohman Supandi, Naoyoshi Nunotani, and Nobuhito Imanaka

   Functional Materials Letters, in press.

4. Particle Size Effect of ZrO_2 Supports on Catalytic Liquid-Phase Oxidation of Phenol over Pt/CeO_2-ZrO_2-Bi_2O_3/ZrO_2 Catalysts

   Abdul Rohman Supandi, Naoyoshi Nunotani, and Nobuhito Imanaka

   Journal of Asian Ceramic Societies, in press.

Supplementary publication

1. Catalytic Liquid-Phase Oxidation of Phenolic Compounds Using Ceria-Zirconia Based Catalysts

   Naoyoshi Nunotani, **Abdul Rohman Supandi**, Pil-Gyu Choi, and Nobuhito Imanaka

   Frontiers in Chemistry, 2018, *6:553*, 1–6.

Chapter 1

Liquid-phase Oxidation of Phenolic Compounds Using Pt/CeO_2-ZrO_2-SnO_2 Supported on SBA-16

1.1. Introduction

To date, it has been reported that the Pt/CZ (Pt/$Ce_{0.90}Zr_{0.10}O_2$) catalyst showed the high activity for the phenol oxidation in the liquid-phase, whose phenol removal percentage reached up to 92% [52]. However, it required severe condition at 160°C under the pressure of 2.0 MPa pure oxygen, and the effective decomposition of phenolic compounds under the moderate condition (low temperatures below 100°C and the atmospheric air pressure) remains the difficult task. To overcome this issue, it is highly required the drastic improvement of oxygen release and storage abilities of the CeO_2-ZrO_2 promoter.

As an effective method for improving the oxygen release and storage abilities of the CeO_2-ZrO_2 solid, SnO_2 doping has been proposed by the Prof. Imanaka's group, to which I belong. SnO_2 doping into the CeO_2-ZrO_2 solid to form solid solution caused the acceleration of oxygen release and storage with contributions of both the redox of Sn^{4+} and Sn^{2+} ions and *n*-type semiconductor property of SnO_2 with electronic conduction [54]. Furthermore, by selecting the mesoporous silica SBA-16 (Santa Barbara Amorphous No. 16) having large surface area as well as a felicitous pore size (Figure 1.1) [57,58] as a support of catalyst, it has been reported that 7wt% Pt/ 16wt% $Ce_{0.68}Zr_{0.17}Sn_{0.15}O_2$/SBA-16 removed 69% of 1,4-dioxane in the liquid-phase at 80°C under the atmospheric air pressure [59].

In this chapter, in order to realize the decomposition of such refractory phenolic compounds under the moderate condition, the catalytic activity of the 7wt% Pt/ 16wt% $Ce_{0.68}Zr_{0.17}Sn_{0.15}O_2$/SBA-16 catalyst was investigated at 80°C under the atmospheric air pressure. As for the target phenolic compounds, phenol and *p*-cresol were selected as the representatives, because they are the common pollutants in the wastewater stream having high toxicity [2–7,60].

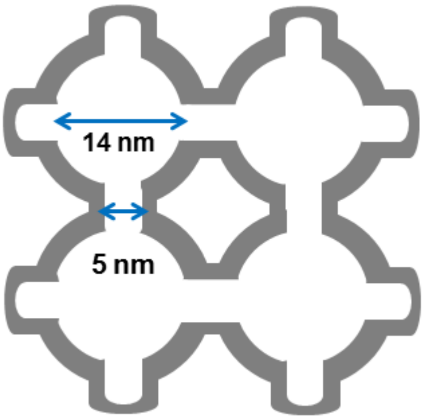

Figure 1.1. Mesoporous structure of SBA-16.

1.2. Experimental Procedure

SBA-16 was prepared using a hydrothermal method according to the previous studies [57]. Pluronic F-127 (1.6 g) was dissolved into the mixture of 0.2 mol·L^{-1} HCl aqueous solution (90 mL) and 1,3,5-trimethylbenzene (1.1 mL), and then stirred at 35°C for 3 h. After that, tetraethoxysilane (7.1 mL) was added, followed by the further stirring at 35°C for 20 h. Subsequently, the mixture was poured into a Teflon bottle and then heated in a sealed brass vessel at 140°C for 24 h. The solid precipitates were collected by suction filtration and washed using water and ethanol. After the drying process at room temperature for 24 h, the powder was calcined at 400°C for 4 h in an air flow (20 mL·min^{-1}).

16wt% $Ce_{0.68}Zr_{0.17}Sn_{0.15}O_2$/SBA-16 samples were synthesized via a co-precipitation process. Aqueous solution of 1.0 mol·L^{-1} $Ce(NO_3)_3$ (0.85 mL) and 0.10 mol·L^{-1} $ZrO(NO_3)_2$ (2.13 mL) were mixed with SnC_2O_4 powder (0.0388 g) in water. After homogenization of the solution, the SBA powder was added and stirred at room temperature for 30 min. By dropwise addition of 5.6vol% NH_3 aqueous solution, the pH of the solution was adjusted to be 11 and further stirred at room temperature for 12 h. The precipitated product was collected by filtration, dried at 80°C, and then calcined at 900°C for 1 h.

Platinum was loaded onto $Ce_{0.68}Zr_{0.17}Sn_{0.15}O_2$/SBA-16 by mixing platinum colloid stabilized in polyvinylpyrrolidone (Pt-PVP, Pt: 4.0wt%, Tanaka Kikinzoku Kogyo) with $Ce_{0.68}Zr_{0.17}Sn_{0.15}O_2$/SBA-16 (0.80 g) in water (40 mL). The loading amount of Pt was adjusted to be 7wt% by using 1.50 g of Pt-PVP, respectively. The mixture was stirred at room temperature for 6 h, followed by the evaporation of the solvent at 180°C. The residue was ground and then calcined at 500°C for 4 h. For comparison, 7wt% Pt/ 16wt% $Ce_{0.80}Zr_{0.20}O_2$/SBA-16 and 7wt% Pt/SBA-16 were also prepared by similar process.

The samples were characterized by X-ray fluorescence analysis (XRF; Supermini200, Rigaku) to confirm the catalysts composition. The mesoporous structure was evaluated by N_2 gas adsorption-desorption analysis, and the pore size and surface area were calculated by using the Barrett-Joyner-Halenda (BJH) and Brunauer-Emmett-Teller (BET) methods, respectively (Tristar 3000, Shimadzu). The crystal structure was identified by X-ray powder diffraction (XRD) measurement using Cu-Kα radiation (40 kV, 30 mA) in the 2θ range between 10 and 70 deg. with a step-scanning mode (SmartLab, Rigaku). For the Rietveld analysis, the XRD data were collected in the range from 10 to 150 deg. with a step width of 0.01 deg. using Cu-Kα radiation (40 kV, 40 mA) (MultiFlex, Rigaku). The structural parameters were determined by Rietveld refinement with a RIETAN-FP program [61]. H_2 temperature programmed reduction (H_2-TPR) was conducted under a 5vol%H_2-95vol%Ar gas flow (50 $mL \cdot min^{-1}$) at the heating rate of 5°$C \cdot min^{-1}$ (BELCAT-B, MicroTracBEL). Subsequently, the oxygen storage capacity (OSC) was investigated using the reduced sample by the pulse-injection method at 500°C (Belcat-B, MicrotracBEL). X-ray photoelectron spectroscopy (XPS) analysis was carried out using Al-Kα radiation (PHI5000 Versa Probe II, ULVAC-PHI), and the spectra were fitted using Shirley background and Gaussian-Lorentzian line shape.

The catalytic oxidation reaction of phenol or *p*-cresol in liquid-phase was carried out using an open-air batch reactor, in which an ethanol-cooled condenser (4°C) was equipped to suppress evaporation (Figure 1.2). The prepared catalyst and 1000 ppm of phenol or *p*-cresol aqueous solution (10 mL) were mixed in the reactor, where the catalyst weight was 0.4 g for phenol (0.04 $g_{cat} \cdot mL^{-1}$) and 0.1 g for *p*-cresol (0.01 $g_{cat} \cdot mL^{-1}$). For the reaction, the mixture was heated in the oil bath and stirred at 80°C under the atmospheric air pressure. After a preset reaction time, aliquot was separated using a centrifuge (Allegra 64R Centrifuge, Beckman Coulter) and mixed with 1000 ppm naphthalene solution in methanol as an internal standard. The remaining concentration in the liquid sample was evaluated by gas chromatography-mass spectrometry (GCMS; GCMS-QP2010 Plus, Shimadzu). The removal percentage was calculated by the following equation:

$$\text{(Removal percentage)} = \frac{C_0 - C}{C_0} \times 100\,\% \tag{1}$$

where C_0 and C are the concentration of the target compound (phenol or *p*-cresol) before and after the reaction, respectively.

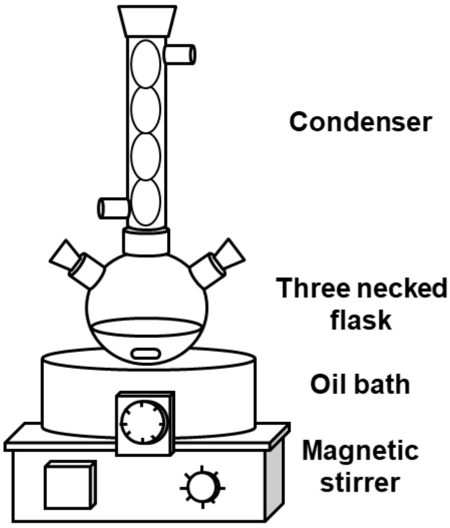

Figure 1.2. Schematic view of the open-system reactor for liquid-phase oxidation.

1.3. Results and Discussion

Table 1.1 shows the measured composition of the 7wt% Pt/ 16wt% $Ce_{0.68}Zr_{0.17}Sn_{0.15}O_2$/SBA-16 (hereafter, denoted as Pt/CZSn/SBA), 7wt% Pt/ 16wt% $Ce_{0.80}Zr_{0.20}O_2$/SBA-16 (Pt/CZ/SBA), and 7wt% Pt/SBA-16 (Pt/SBA) catalysts. The measured compositions of the catalysts were in good agreement with the feed values within the experimental error.

Table 1.1. Composition measured by XRF of the Pt/SBA, Pt/CZ/SBA, and Pt/CZSn/SBA catalysts

Catalyst	Measured composition	Surface area ($m^2 \cdot g^{-1}$)
Pt/SBA	7.0wt% Pt/SBA-16	456
Pt/CZ/SBA	6.8wt% Pt/ 16wt% $Ce_{0.80}Zr_{0.20}O_2$/SBA-16	279
Pt/CZSn/SBA	6.8wt% Pt/ 16wt% $Ce_{0.69}Zr_{0.17}Sn_{0.14}O_2$/SBA-16	257

Figure 1.3(a) shows the N_2 adsorption-desorption isotherms of the prepared catalysts with the data of SBA-16 (SBA). The isotherm pattern of SBA showed the distinctiveness of hysteresis curves that corresponding to the type IV according to IUPAC (International Union of Pure and Applied Chemistry) classification, which is typical for the mesoporous material [62]. Since the similar patterns were observed for the Pt/SBA, Pt/CZ/SBA, and Pt/CZSn/SBA catalysts, the mesoporous structure of SBA-16 was still maintained after the loading of Pt and the promoter. Figure 1.3(b) shows the BJH pore size distribution of the prepared catalysts and SBA. While the main pore size of SBA was estimated to be ca. 14 nm, the loading of Pt caused a decrease of the pore size to ca. 13 nm. In addition, the loading of promoter further decreased the pore size down to ca. 11 nm, while the pore size of Pt/CZ/SBA and Pt/CZSn/SBA were similar. The decrease of pore volume itself was possibly caused by a dilution effect due to the loading of Pt and the promoter. While the surface area of SBA was confirmed to be 648 $m^2 \cdot g^{-1}$, the loading of Pt and the promoter caused a decrease of the surface area as listed in Table 1.1.

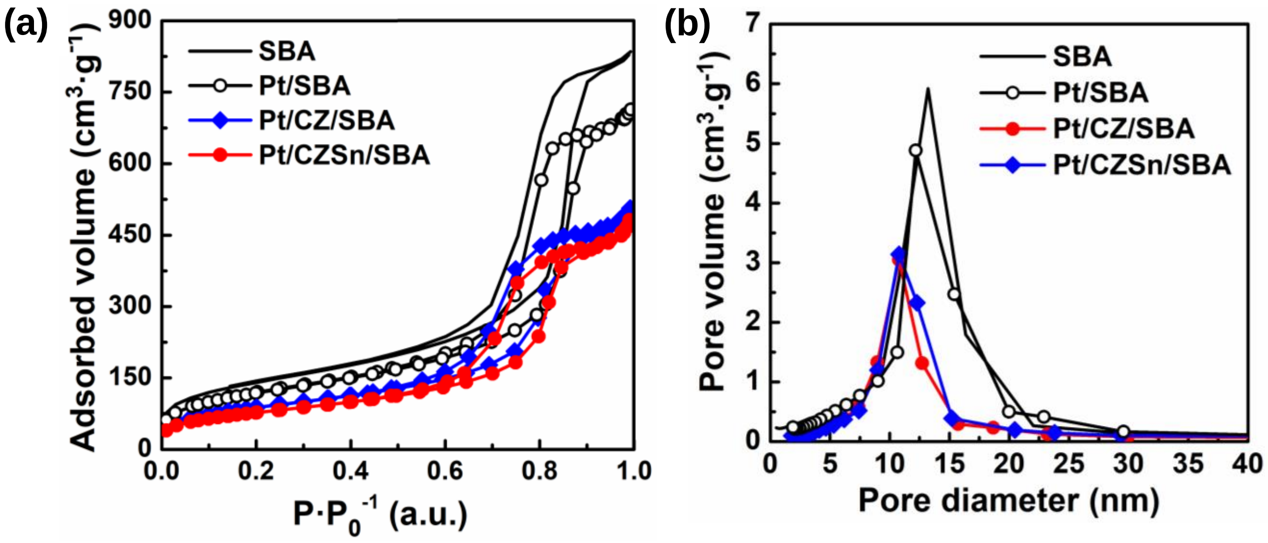

Figure 1.3. (a) N_2 adsorption-desorption isotherm curves and (b) BJH pore size distribution of the Pt/SBA, Pt/CZ/SBA, and Pt/CZSn/SBA catalysts with the data of SBA.

Figure 1.4 shows the XRD patterns of Pt/SBA, Pt/CZ/SBA, and Pt/CZSn/SBA. For Pt/SBA, the peaks were identified only as SBA-16 and Pt. In the cases of the catalysts with the promoter, four diffraction peaks, assigned as the cubic fluorite-type structure, were additionally observed, where no impurity phase was detected. In addition, the peaks of the fluorite-type phase in Pt/CZSn/SBA were shifted toward higher angles compared to the case of Pt/CZ/SBA, suggesting that the Ce^{4+} (0.111 nm, coordination number [CN] = 8 [63]) and Zr^{4+} (0.098 nm, CN = 8 [63]) sites were replaced by the smaller ionic-radius of Sn^{4+} (0.095 nm, CN = 8 [63]).

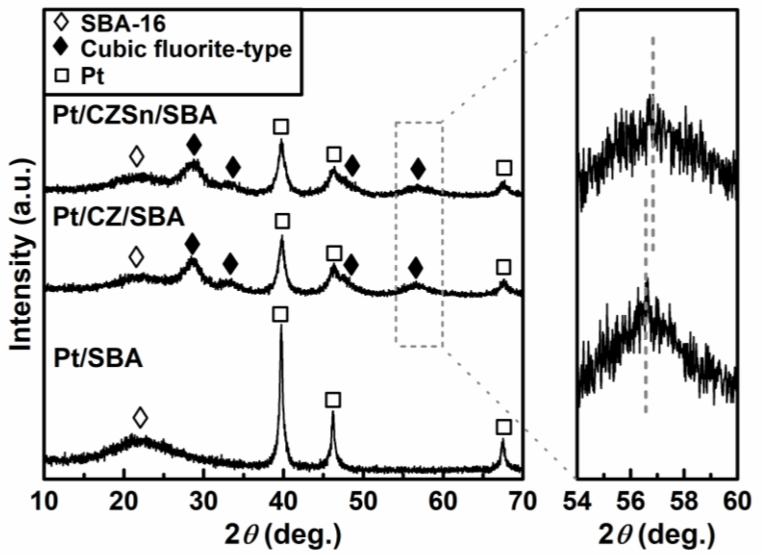

Figure 1.4. XRD patterns of the Pt/SBA, Pt/CZ/SBA, and Pt/CZSn/SBA catalysts.

To investigate the effect of SnO_2 on the lattice in detail, the crystal structure of the cubic fluorite-type phase was analyzed by Rietveld refinement using the XRD data of 16wt% $Ce_{0.68}Zr_{0.17}Sn_{0.15}O_2$/SBA (CZSn/SBA) and 16wt% $Ce_{0.80}Zr_{0.20}O_2$/SBA (CZ/SBA). The results of the refinements are shown in Figure 1.5, and the structural parameters of the fluorite-type structure are summarized in Table 1.2. Here, the XRD pattern of the SBA-16 sample was used for the correction of background, and the occupation of the cations were used the estimated values obtained from the XRF measurement. The lattice constant of $Ce_{0.69}Zr_{0.17}Sn_{0.14}O_2$ (0.5422 nm) was lower than that of $Ce_{0.80}Zr_{0.20}O_2$ (0.5429 nm); that is, the lattice shrinkage of the fluorite-type structure by introducing the small ionic-size of Sn^{4+} into the CeO_2-ZrO_2 lattice was clearly demonstrated. The oxygen occupation for $Ce_{0.80}Zr_{0.20}O_2$ were 0.928, indicating the partial reduction of Ce^{4+} to Ce^{3+}, where the Ce^{4+}:Ce^{3+} ratio was estimated to be 82:18. Since the oxygen occupation for $Ce_{0.69}Zr_{0.17}Sn_{0.14}O_2$ (0.909) was lower than the $Ce_{0.80}Zr_{0.20}O_2$ case (0.928), the SnO_2 introduction also caused the generation of oxygen vacancies, which might be favorable for the oxide ion migration during the oxygen release and storage processes. Under the assumption of the same Ce^{4+}:Ce^{3+} ratio for $Ce_{0.69}Zr_{0.17}Sn_{0.14}O_2$ as $Ce_{0.80}Zr_{0.20}O_2$, the Sn^{4+}:Sn^{2+} ratio can be calculated as 59:41.

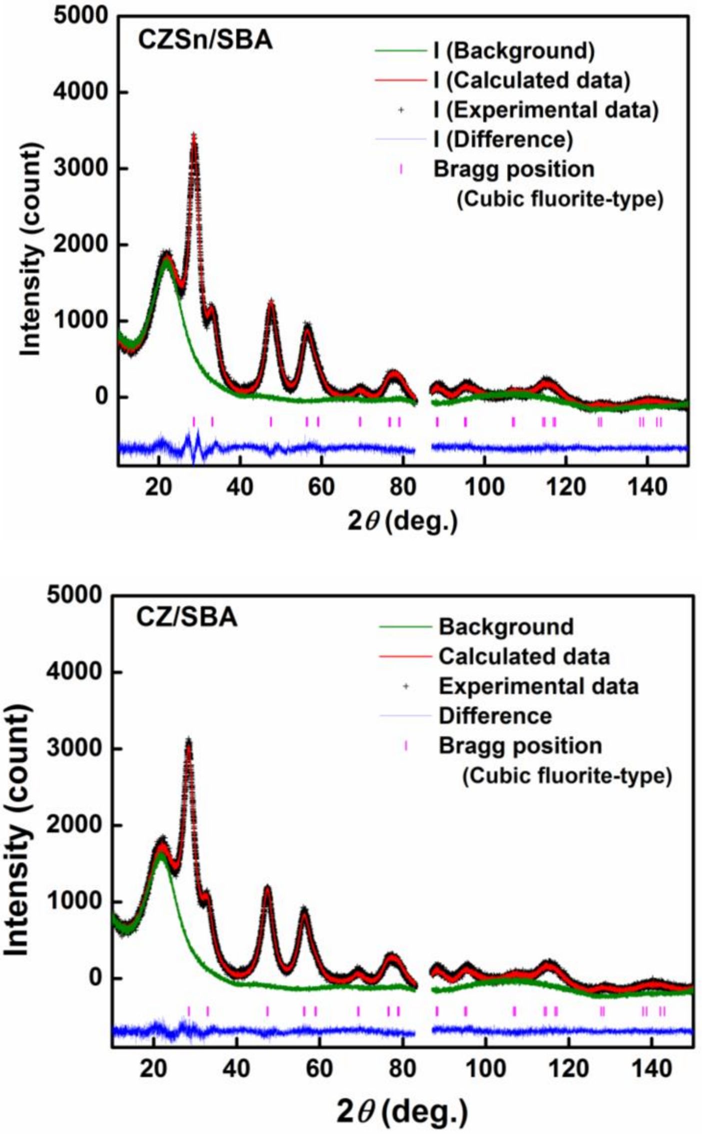

Figure 1.5. Results of the Rietveld analyses of CZSn/SBA and CZ/SBA.

Table 1.2. Structural parameters of the cubic fluorite-type structure obtained from the Rietveld analysis

Sample	Lattice constant (nm)	Atom	Wyckoff position	Occupation	*x*	*y*	*z*	*B* (Å^2)
CZSn/SBA	0.5422(1)	Ce	4*a*	0.69	0	0	0	1
		Zr	4*a*	0.17	0	0	0	1
		Sn	4*a*	0.14	0	0	0	1
		O	8*c*	0.909(1)	1/4	1/4	1/4	1
Space group: $Fm\overline{3}m$, $R_{\mathrm{wp}} = 4.81\%$, $S = 1.37$								
CZ/SBA	0.5429(1)	Ce	4*a*	0.8	0	0	0	1
		Zr	4*a*	0.2	0	0	0	1
		O	8*c*	0.928(1)	1/4	1/4	1/4	1
Space group: $Fm\overline{3}m$, $R_{\mathrm{wp}} = 4.61\%$, $S = 1.29$								

To investigate the oxygen release and storage abilities of the promoters, H_2-TPR and OSC measurements were performed. Figure 1.6 shows the H_2-TPR profiles of CZSn/SBA and CZ/SBA. CZ/SBA had one broad peak at 451°C owing to the reduction of Ce^{4+}. For CZSn/SBA, the peak was split into two which were assigned as the surface (at 320°C) and bulk reductions (at 376°C) of Ce^{4+}, respectively, and the reduction peak top temperature was lowered by introducing SnO_2 into CeO_2-ZrO_2. After the H_2-TPR analysis, the OSC measurement was carried out, and the results are listed in Table 1.3 with the first reduction peak top temperature obtained by H_2-TPR measurement. An obvious increase of the OSC value was observed for CZSn/SBA. Both the lower reduction temperature and high OSC value of the CZSn/SBA clearly indicated that the oxygen release and storage abilities were improved by the SnO_2 introduction, because of the synergistic redox cycles between $Ce^{4+/3+}$ and $Sn^{4+/2+}$ and *n*-type semiconductor properties of SnO_2 [54].

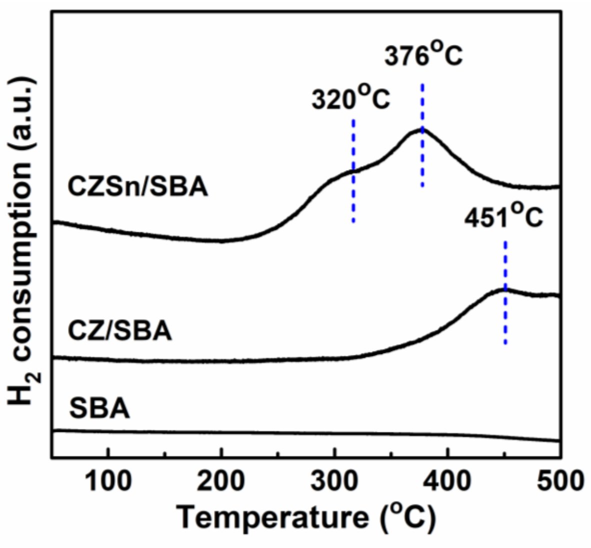

Figure 1.6. H_2-TPR profiles of SBA, CZ/SBA, and CZSn/SBA.

Table 1.3. First reduction peak top temperature and OSC value of the CZ/SBA and CZSn/SBA samples

Sample	Reduction temperature (°C)	OSC value ($mmol\cdot g^{-1}$)
CZSn/SBA	320	0.098
CZ/SBA	451	0.031

For Pt/CZSn/SBA, Pt/CZ/SBA, and Pt/SBA, the oxidation state of surface Pt were investigated by XPS. Figure 1.7 presents the XPS results of the Pt 4f core level, and fitting parameters are summarized in Table 1.4. For all the catalysts, the binding energies were fitted by the Pt $4f_{7/2}$ and $4f_{5/2}$ of Pt^{2+} and Pt^0, and the $Pt^{2+}/(Pt^0+Pt^{2+})$ ratios were estimated from the peak areas related to Pt^{2+} and Pt^0 in the XPS spectra (Table 1.4). Pt/CZSn/SBA and Pt/CZ/SBA have the higher $Pt^{2+}/(Pt^0+Pt^{2+})$ ratio values compared to Pt/SBA. In particular, the $Pt^{2+}/(Pt^0+Pt^{2+})$ ratio of Pt/CZSn/SBA was higher than that of Pt/CZ/SBA. These results indicate that the promoter contributed to the oxidation of the surface Pt species, where it was reported that the reducibility of CeO_2 generated the oxidized Pt species: $Pt^0 + 2Ce^{4+} \rightarrow Pt^{2+} + 2Ce^{3+}$ [64].

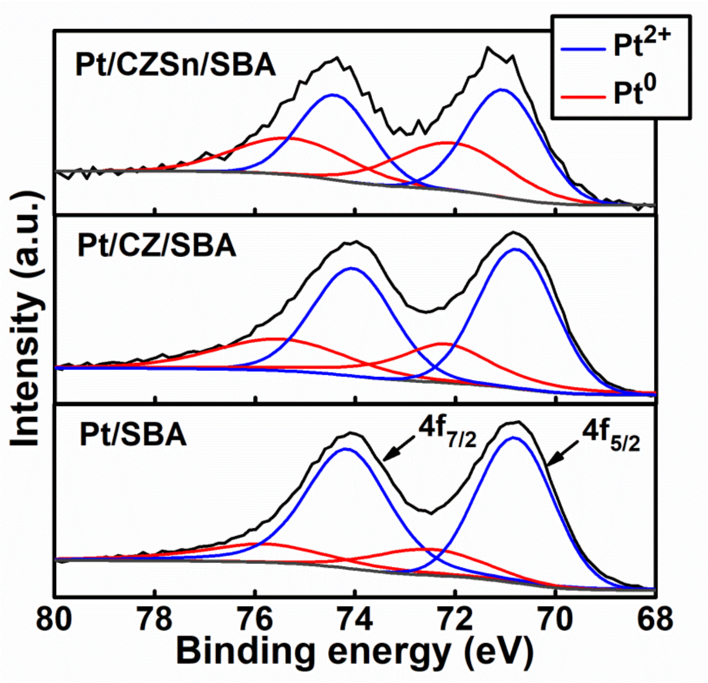

Figure 1.7. The Pt 4f core level XPS spectra of the Pt/SBA, Pt/CZ/SBA, and Pt/CZSn/SBA catalysts.

Table 1.4. Fitting parameters of the Pt 4f XPS spectra for the Pt/SBA, Pt/CZ/SBA, and Pt/CZSn/SBA catalysts

Catalyst	Peak	Peak position (eV)	FWHM (eV)	Area (%)	$Pt^{2+}/(Pt^0+Pt^{2+})$ ratio (%)
Pt/CZSn/SBA (χ^2 = 0.014)	Pt^{2+} $4f_{5/2}$	75.4	2.7	17.8	40
	Pt^0 $4f_{5/2}$	74.3	1.7	26.1	
	Pt^{2+} $4f_{7/2}$	72.1	2.7	22.7	
	Pt^0 $4f_{7/2}$	71.0	1.7	33.4	
Pt/CZ/SBA (χ^2 = 0.002)	Pt^{2+} $4f_{5/2}$	75.5	3.1	15.0	34
	Pt^0 $4f_{5/2}$	74.1	1.8	28.1	
	Pt^{2+} $4f_{7/2}$	72.2	3.1	19.6	
	Pt^0 $4f_{7/2}$	70.8	1.8	37.3	
Pt/SBA (χ^2 = 0.002)	Pt^{2+} $4f_{5/2}$	75.8	3.0	9.8	22
	Pt^0 $4f_{5/2}$	74.2	1.9	34.7	
	Pt^{2+} $4f_{7/2}$	72.5	2.6	12.6	
	Pt^0 $4f_{7/2}$	70.8	1.8	42.9	

The phenol removal percentages as a function of reaction time are shown in Figure 1.8. Even only for SBA, 19% of phenol was removed after 6 h reaction, which suggests that phenol was adsorbed onto SBA and/or evaporated during the reaction. After the reaction for 6 h, while the Pt/SBA catalyst removed 76% of phenol, the presence of the CeO_2-ZrO_2 promoter increased the phenol removal percentage to 85%, suggesting that the CeO_2-ZrO_2 promoter facilitated the oxidation of phenol on the Pt activator. The highest phenol removal percentage was obtained for the Pt/CZSn/SBA catalyst, whose phenol removal percentage rose to 91% after the reaction for 6 h. Since the activity of Pt/CZSn/SBA was higher than that of Pt/CZ/SBA regardless of the small surface area (Pt/CZSn/SBA: 257 $m^2.g^{-1}$, Pt/CZ/SBA: 279 $m^2.g^{-1}$), the high catalytic activity of Pt/CZSn/SBA was likely due to the introduction of SnO_2 into CeO_2-ZrO_2 lattice that improved the oxygen release and storage abilities to facilitate the generation of Pt^{2+} which is more active in phenol oxidation than Pt^0 [64]. While the oxidation of phenol involved the reduction of Pt^{2+} to Pt^0, the re-oxidation process of Pt^0 was considered to be accelerated owing to a successive supply of active oxygen species from the promoter [64]. Here, the promoter might be oxidized by oxygen molecules, dissolved in the liquid-phase from atmospheric air, because the catalytic reaction was conducted in the open air system. The phenol removal percentage of Pt/CZSn/SBA (91%) after the reaction for 6 h was comparable with that of the previously reported Pt/CZ catalyst (92%) whose condition was 160°C under 2.0 MPa (pure oxygen) for 3 h [52], meaning that the present Pt/CZSn/SBA catalyst possesses the considerably high catalytic activity because the reaction condition is obviously moderate (80°C, the atmospheric air pressure). CO_2 and H_2O are seemed to be the final products of phenol oxidation; however, CO_2 could not be trapped for GC-MS measurement due to the open-air system reaction, and H_2O was mixed with solvent. In the solution after the reaction for 6 h, benzoquinone was detected as intermediate of phenol oxidation, and its concentration for Pt/CZSn/SBA (~42 ppm) was lower than that for Pt/CZ/SBA (~82 ppm) and Pt/SBA (~100 ppm). In addition, acetic acid (~172 ppm) was detected only for Pt/SBA. For the previously reported Pt/CZ, quinone and carboxylic acid were also detected as intermediates.

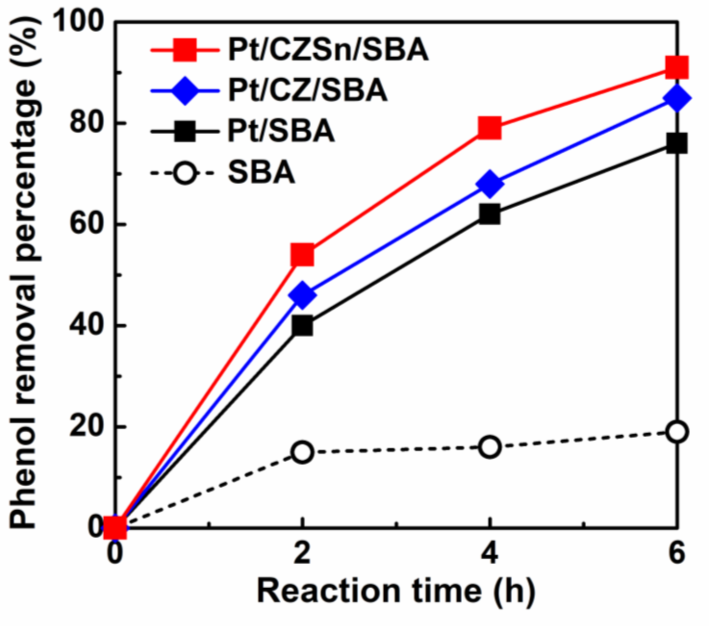

Figure 1.8. Phenol removal percentages as a function of reaction time.
(1000 ppm phenol 10 mL, 0.04 $g_{cat}\cdot mL^{-1}$, 80°C, atmospheric air pressure)

Figure 1.9 depicts the *p*-cresol removal percentage for Pt/CZSn/SBA with the data of Pt/CZ/SBA, Pt/SBA, and SBA. The order of the catalytic activity was: Pt/CZSn/SBA > Pt/CZ/SBA > Pt/SBA, and this tendency was same as the phenol removal percentage. In other words, the introduction of CZSn was also effective for the *p*-cresol oxidation, and the complete removal of *p*-cresol was achieved after the reaction for 4 h under the atmospheric air pressure. As the catalyst effective for the removal of *p*-cresol, Ag/Al_2O_3-ZrO_2 catalyst has been reported; however, it needed severe conditions of 160°C and 1.5 MPa (pure oxygen) and longer reaction time (6 h) for the complete *p*-cresol removal [65]. Thus, it was revealed that the Pt/CZSn/SBA catalyst showed the high efficiency under the moderate conditions. Furthermore, no intermediate was detected in the solution after the reaction for 4 h using Pt/CZSn/SBA, while some intermediates such as methylcatechol, hydroxybenzyl alcohol were found in the case of previously reported Ag/Al_2O_3-ZrO_2.

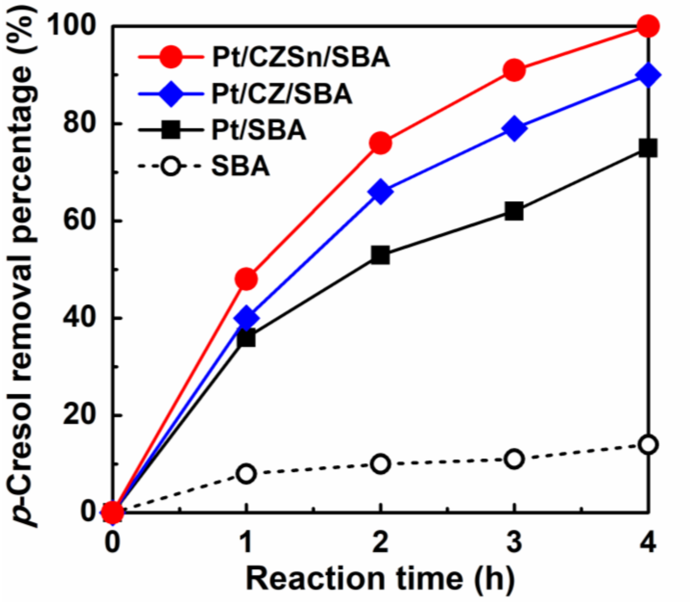

Figure 1.9. *p*-Cresol removal percentages as a function of reaction time.

(1000 ppm phenol 10 mL, 0.01 $g_{cat}\cdot mL^{-1}$, 80°C, atmospheric air pressure)

1.4. Conclusion

In this chapter, for the decomposition of phenolic compounds under moderate condition, the 7wt% Pt/ 16wt% $Ce_{0.68}Zr_{0.17}Sn_{0.15}O_2$/SBA-16 catalyst was applied. By applying the CeO_2-ZrO_2-SnO_2 as a promoter which supply active oxygen to the Pt activator, the oxygen release and storage abilities of the promoter was greatly improved due to the synergistic redox cycles between $Ce^{4+/3+}$ and $Sn^{4+/2+}$ and *n*-type semiconductor properties of SnO_2. As a result of successful improvement in oxygen release and storage ability, the 7wt% Pt/ 16wt% $Ce_{0.68}Zr_{0.17}Sn_{0.15}O_2$/SBA-16 catalyst realized a 91% removal of phenol after the reaction for 6 h at 80°C under the atmospheric air pressure, which is quite moderate condition compared with that of the previously reported Pt/CZ catalyst (160°C, 2.0 MPa of pure oxygen pressure) required for removing 92% of phenol after 3 h. For the *p*-cresol oxidation, the present catalyst could realize a complete removal after the reaction for 4 h at 80°C under the atmospheric air pressure, while the previously reported Ag/Al_2O_3-ZrO_2 catalyst required more severe reaction condition (160°C, 1.5 MPa) and long reaction time (6 h) to completely remove *p*-cresol.

Chapter 2

Liquid-phase Oxidation of Phenol Using Pt/CeO_2-ZrO_2-SnO_2 Supported on ZrO_2/SBA-16

2.1. Introduction

In Chapter 1, while the phenol removal at the moderate condition of 80°C under the atmospheric air pressure was successfully realized by using the 7wt% Pt/ 16wt% $Ce_{0.68}Zr_{0.17}Sn_{0.15}O_2$/SBA-16 catalyst, its removal percentage was 91% after the reaction for 6 h in maximum and the complete removal was not recognized.

Therefore, this chapter 2 aims to realize the complete phenol removal by the further enhancement of the catalytic activity. To this end, the acidity of support was focused. As schematically illustrated in Figure 2.1, the electron withdrawing of the Lewis acidic sites should generate the strong interaction with supported metal oxide, in this case, promoter. This strong bonding is expected to suppress the aggregation of promoter, meaning that the surface active sites to release and store the oxygen species may be increased. As an example, increase of the acidity of the support has been reported to enhance the dispersion of the supported materials [66,67] for the ZrO_2 loaded SiO_2 support and improved the dispersibility and the reducibility of the supported metal oxide, such as vanadium oxide and molybdenum oxide [55,56].

Accordingly, the ZrO_2 was loaded on SBA-16 (ZrO_2/SBA-16) supports prior to the supporting of Pt and CeO_2-ZrO_2-SnO_2 in order to improve the oxygen release and storage abilities of the CeO_2-ZrO_2-SnO_2 promoter by suppressing their aggregation. Based on this concept,

Pt/CeO_2-ZrO_2-SnO_2/ZrO_2/SBA-16 catalysts were synthesized, and their catalytic activities for the phenol removal were investigated.

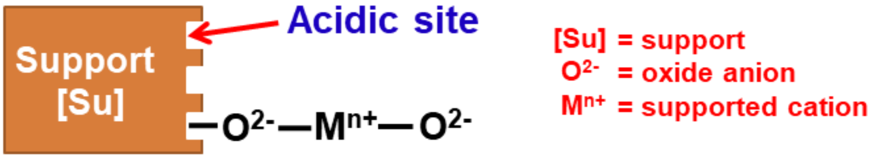

Figure 2.1. Schematic illustration of the interaction between supports having Lewis acidic site and the supported metal oxide.

2.2. Experimental Procedure

ZrO_2 was loaded onto SBA by using impregnation method followed by the hydrolysis treatment. SBA (1.00 g) was dispersed into aqueous solution of $ZrO(NO_3)_2$, prepared by dissolving a certain amount of $ZrO(NO_3)_2$ powder into water (20 mL). The mixture was stirred at room temperature for 6 h and then heated at 130°C to evaporate the solvent. The dried samples were hydrolized by NH_3/H_2O vapor exposure treatment; i.e., the sample placed in the vial was put into a beaker glass equipped with a cap that contains 14vol% NH_3 aqueous solution as illustrated in Figure 2.2, and then heated at 70°C for 6 h. The hydrolized sample was dried at 80°C, and calcined at 500°C for 6 h under an air flow (20 $mL\cdot min^{-1}$) to obtain the $x$wt% ZrO_2/SBA-16 supports. Here, the ZrO_2 loading amount (x) was adjusted to 12–36wt%.

The $Ce_{0.68}Zr_{0.17}Sn_{0.15}O_2$ loading onto $x$wt% ZrO_2/SBA-16 was conducted by the same method outlined in Chapter 1; i.e., the co-precipitation process followed by the calcination at 900°C. The Pt loading was also carried out using the impregnation procedure according to Chapter 1, where $Ce_{0.68}Zr_{0.17}Sn_{0.15}O_2$ and Pt loading amount were adjusted to be 16wt% and 7wt%, same as Chapter 1.

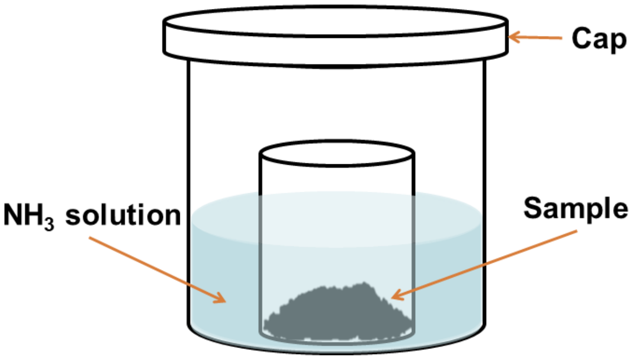

Figure 2.2. Schematic view of the hydrolysis treatment during the *x*wt% ZrO_2/SBA-16 preparation.

The obtained samples were characterized by using XRF analysis (Supermini200, Rigaku) and XRD measurement (SmartLab, Rigaku). The Raman spectrum was obtained using the 532 nm laser as an excitation source, operated at the power of 100 mW (NRS-3100, Jasco). N_2 gas adsorption-desorption measurement was conducted, and the pore size distribution and the surface area were evaluated using the BJH and BET methods, respectively (Tristar 3000, Shimadzu). The concentration of the acidic sites was estimated from the temperature-programmed desorption using NH_3 (NH_3-TPD), assuming that one NH_3 molecule adsorbs on one acidic site. The sample was exposed to the flow of 0.5vol%NH_3-99.5vol%N_2 (50 $mL\cdot min^{-1}$) at 50°C for 30 min. After evacuation at 50°C for 15 min, the catalyst was heated under a flow of He at the rate of 10°C·min^{-1} and the desorbed gas was monitored (BELCAT-B, MicrotracBEL). H_2-TPR was carried out in 5vol%H_2-95vol%Ar flow (50 $mL\cdot min^{-1}$) with the heating rate of 5°C·min^{-1}, followed by the OSC measurement using pulse injection method at 500°C (BELCAT-B, MicrotracBEL). X-ray photoelectron spectroscopy (XPS) analysis was performed to investigate the oxidation state of Pt at room temperature using Al-Kα radiation (PHI5000 Versa Probe II, ULVAC-PHI), and the spectra were fitted using Shirley background and Gaussian-Lorentzian line shape.

The liquid-phase oxidation of phenol was carried out according to Chapter 1. After the reaction, the catalyst was collected, dried at 80°C, and then reused for the liquid-phase oxidation to examine the catalyst reusability test, where the amount of the catalyst in the solution was fixed to be 0.04 $g_{cat}\cdot mL^{-1}$.

2.3. Results and Discussion

For the *x*wt% ZrO_2/SBA-16 ($ZrO_2(x)$/SBA) supports, the compositions were confirmed to have a good agreement with the feed compositions (Table 2.1). The N_2 adsorption-desorption isotherm curves and BJH pore size distribution of the $ZrO_2(x)$/SBA supports with the data of SBA are shown in Figure 2.3. The curves of $ZrO_2(x)$/SBA were similar hysteresis loop shape to the SBA, indicating that the mesoporous structure of SBA-16 was preserved [62]. In the case of the BJH pore size, the loading of ZrO_2 slightly decreased the pore size of SBA to ca. 13 nm, possibly due to the insertion of small particle size of ZrO_2 inside the pore. Meanwhile, the pore volume was monotonically decreased after the loading of ZrO_2, likely due to the dilution effect caused by the loading of ZrO_2. In addition, the loading of ZrO_2 also caused a decrease of the surface area, and it was monotonically decreased with the increase of the ZrO_2 loading amount (Table 2.1).

Table 2.1. Measured compositions of the $ZrO_2(x)$/SBA supports

Sample	Measured composition	Surface area ($m^2\cdot g^{-1}$)
SBA	-	648
ZrO_2(12)/SBA	11.2wt% ZrO_2/SBA-16	310
ZrO_2(18)/SBA	18.3wt% ZrO_2/SBA-16	298
ZrO_2(24)/SBA	23.1wt% ZrO_2/SBA-16	290
ZrO_2(30)/SBA	29.5wt% ZrO_2/SBA-16	273
ZrO_2(36)/SBA	34.9wt% ZrO_2/SBA-16	251

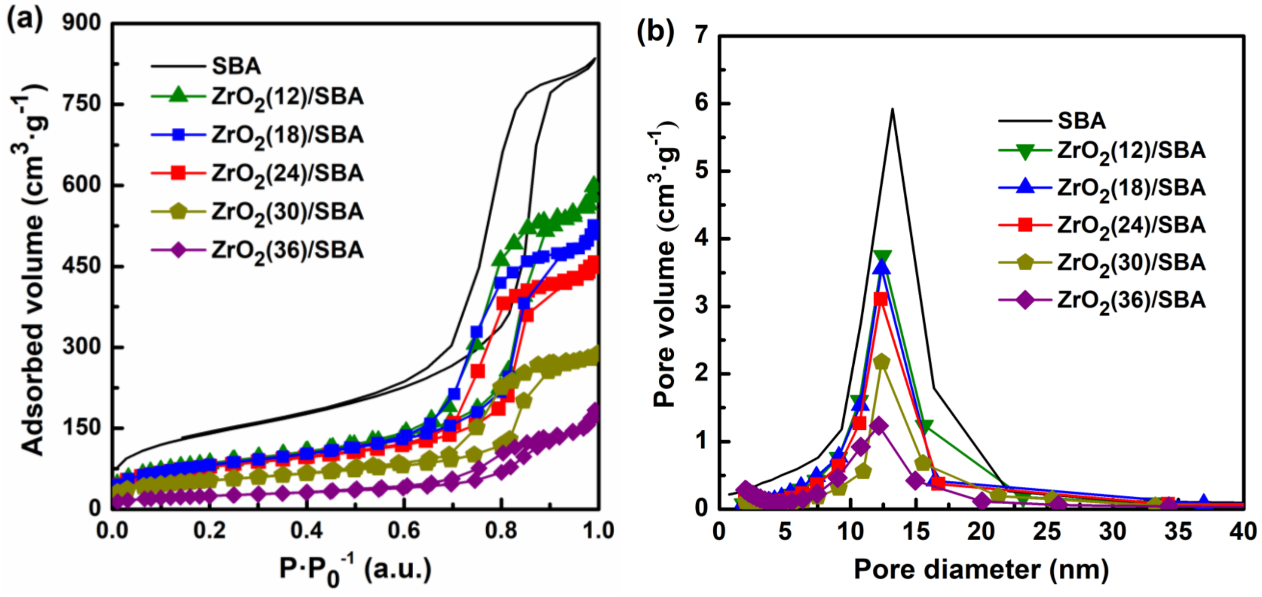

Figure 2.3. (a) N_2 adsorption-desorption isotherm linear curves and (b) BJH pore size distribution of the $ZrO_2(x)$/SBA supports.

Figure 2.4 shows the XRD patterns and the Raman spectra of the $ZrO_2(x)$/SBA supports. In the case of XRD patterns, while SBA has only a broad peak at ca. 22 deg., an additional broad peak with low-intensty, which can be assigned to be tetragonal ZrO_2 phase, was observed at ca. 30 deg. for $ZrO_2(x)$/SBA [68]. The formation of the tetragonal ZrO_2 phase was also confirmed by the Raman spectrum for the support with $x = 36$, where the peaks at 291, 472, and 642 cm^{-1} are corresponding to tetragonal ZrO_2 [69]. Meanwhile, the obvious Raman peaks were not observed for the $ZrO_2(x)$/SBA supports ($x \leq 30$) due to the low crystallinity. Here, the strong interaction between ZrO_2 and SiO_2 might cause the suppression of the crystal growth, resulting in the low crystallinity of ZrO_2 for $ZrO_2(x)$/SBA [67]. These results also suggest that ZrO_2 was highly dispersed onto SBA.

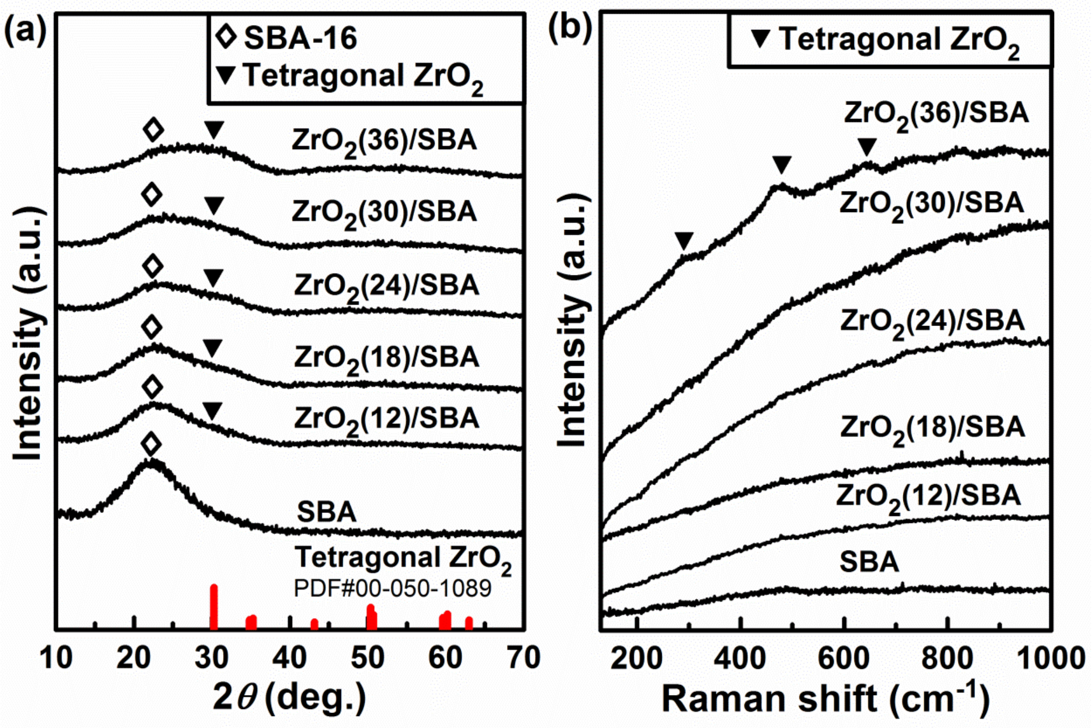

Figure 2.4. (a) XRD patterns and (b) Raman spectra of the $ZrO_2(x)$/SBA supports.

Figure 2.5 displays the NH_3-TPD profiles of the $ZrO_2(x)$/SBA supports. For SBA, two peaks were observed at ca. 120°C and ca. 300°C, corresponding to the weak and strong acidic sites, respectively. The loading of ZrO_2 onto SBA remarkably increased the peak intensities. To investigate the effect of the ZrO_2 loading amount on the acidity of $ZrO_2(x)$/SBA, the concentration of the acidic sites was estimated from the NH_3-TPD profile, and the results are presented in Figure 2.6. With the increase of x, the concentration of the acidic sites was increased up to $x = 24$, regardless of the decrease of the surface area (Table 2.1). For $x > 24$, the acidity decreased with increasing x, due to the aggregation of ZrO_2 on the SBA surface to grow the ZrO_2 particle. Lager ZrO_2 particle size results in the decrease of the surface Zr^{4+} ion in ZrO_2 which is known as the acidic site. Thus, the highest acidity was obtained for the ZrO_2(24)/SBA ($x = 24$) support.

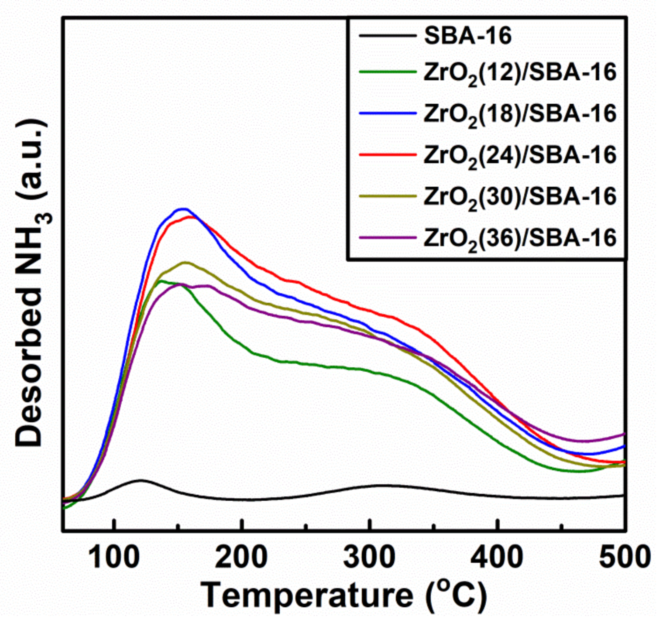

Figure 2.5. NH_3-TPD profiles of the ZrO_2(*x*)/SBA supports.

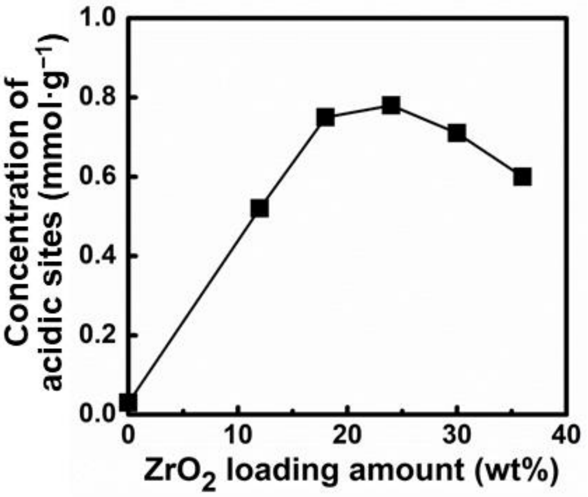

Figure 2.6. Effect of the ZrO_2 loading amount on the concentration of the acidic sites in the ZrO_2(*x*)/SBA supports.

To investigate the oxygen release and storage abilities of the 16wt% $Ce_{0.68}Zr_{0.17}Sn_{0.15}O_2$/ *x*wt% ZrO_2/SBA-16 (CZSn/ZrO_2(*x*)/SBA) samples, the H_2-TPR measurement was conducted, followed by the OSC measurement. Figure 2.7 shows the H_2-TPR profiles of CZSn/ZrO_2(*x*)/SBA. All samples had two peaks suggesting the surface and bulk reductions of CeO_2-ZrO_2-SnO_2 at lower and higher temperatures, respectively. Figure 2.8 presents the ZrO_2 loading amount dependencies of the first reduction temperature and the OSC value. In the range with $x \leq 24$, the first reduction temperature was lowered and the OSC value was increased with increasing *x*, indicating that the oxygen release and storage abilities were enhanced. These improvements might be affected by the phenomenon that ZrO_2/SBA with high acidity led to the high dispersibility of the CeO_2-ZrO_2-SnO_2 promoter, similar to the previous studies [55,56]. For $x > 24$, oxygen release and storage abilities were decreased, likely due to the decrease of the concentration of the acidic sites as well as the surface area. Thus, the CZSn/ZrO_2(24)/SBA sample showed the highest oxygen release and storage abilities among the prepared samples.

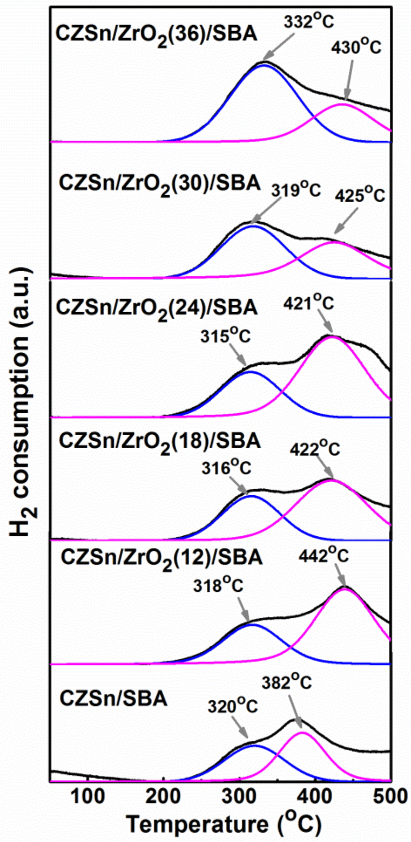

Figure 2.7. H_2-TPR profiles of CZSn/ZrO_2(*x*)/SBA.

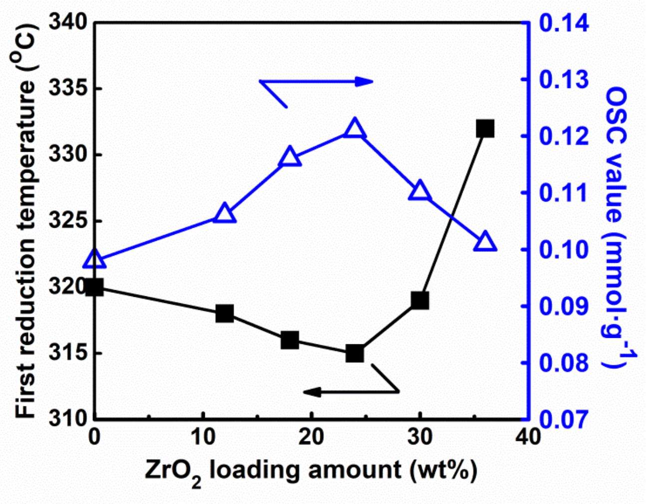

Figure 2.8. Dependence of the ZrO_2 loading amount (x) on first reduction temperature and OSC value of CZSn/ZrO_2(x)/SBA.

Figure 2.9 depicts the XRD patterns of the 7wt% Pt/ 16wt% $Ce_{0.68}Zr_{0.17}Sn_{0.15}O_2$/ $x$wt% ZrO_2/SBA-16 (Pt/CZSn/ZrO_2(x)/SBA) catalysts with the data of 7wt% Pt/ 16wt% $Ce_{0.68}Zr_{0.17}Sn_{0.15}O_2$/SBA-16 (Pt/CZSn/SBA). In comparison with the XRD patterns of ZrO_2(x)/SBA (Figure 2.4(a)), Pt/CZSn/ZrO_2(x)/SBA have additional peaks, corresponding to Pt and the cubic fluorite-type phase of CeO_2-ZrO_2-SnO_2.

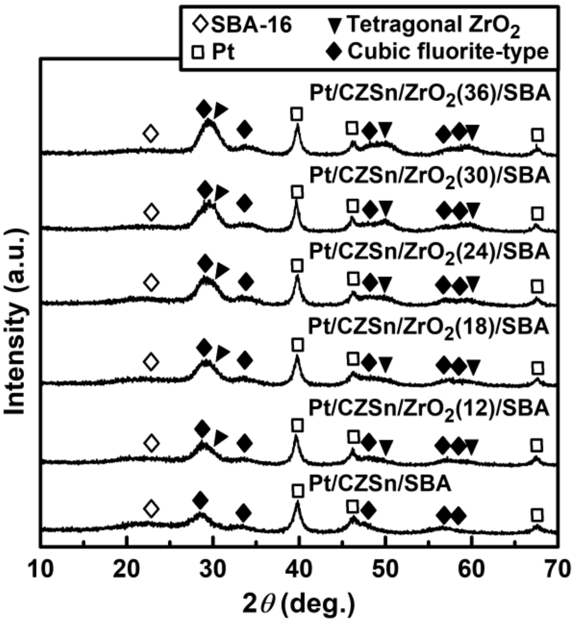

Figure 2.9. XRD patterns of the Pt/CZSn/ZrO_2(x)/SBA catalysts.

Figure 2.10 shows the N_2 adsorption-desorption isotherm curves and the BJH pore size distribution of the Pt/CZSn/ZrO_2(*x*)/SBA catalysts. The isotherm curves of the catalysts have the hysteresis loop shape as type IV, meaning that the mesoporous structure of SBA-16 were still preserved even after the loading of Pt, CZSn, and ZrO_2 [62], while the loading of ZrO_2 slightly decreased the pore size compared to Pt/CZSn/SBA. Table 2.2 shows the BET surface areas of Pt/CZSn/ZrO_2(*x*)/SBA. The introduction of Pt and CZSn decreased the surface areas compared to those of ZrO_2(*x*)/SBA (Table 2.1). Here, the trend of the relation between the surface area and the ZrO_2 loading amount (*x*) in Pt/CZSn/ZrO_2(*x*)/SBA is similar to the ZrO_2(*x*)/SBA case (Table 2.1).

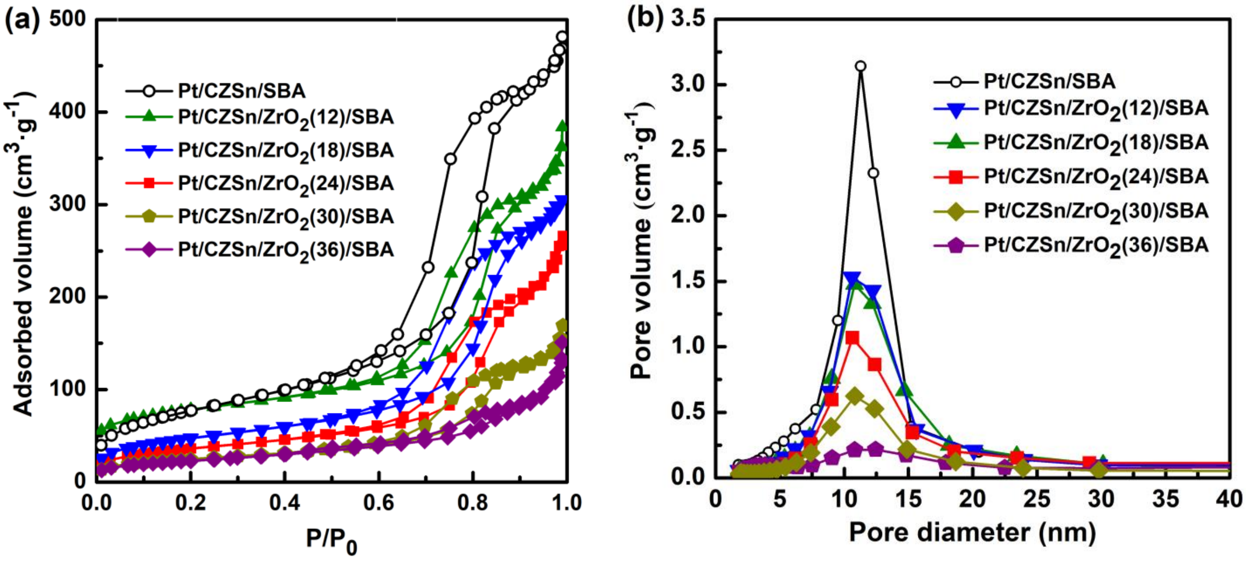

Figure 2.10. (a) N_2 adsorption-desorption isotherm linear curves and (b) BJH pore size distribution of the Pt/CZSn/ZrO_2(*x*)/SBA catalysts.

Table 2.2. Surface area of the Pt/CZSn/ZrO_2(*x*)/SBA catalysts

Catalyst	Surface area ($m^2 \cdot g^{-1}$)
Pt/CZSn/SBA	257
Pt/CZSn/ZrO_2(12)/SBA	181
Pt/CZSn/ZrO_2(18)/SBA	176
Pt/CZSn/ZrO_2(24)/SBA	138
Pt/CZSn/ZrO_2(30)/SBA	96
Pt/CZSn/ZrO_2(36)/SBA	89

In order to investigate the valence state of Pt, the XPS spectra of Pt 4f core-levels were measured. The spectra and the refinement parameters are shown in Figure 2.11 and Table 2.3. The XPS spectra of Pt 4f core-levels demonstrated that both Pt^0 and Pt^{2+} existed in the prepared catalysts. The $Pt^{2+}/(Pt^0+Pt^{2+})$ ratio was estimated from the XPS peak areas, and the results are summarized in Table 2.3. With increasing x, the $Pt^{2+}/(Pt^0+Pt^{2+})$ ratio increased up to $x = 24$, while further increase in x caused the decrease of oxidized Pt. This result also supports an idea that the high oxygen release and storage abilities of the promoter might facilitate the generation of the oxidized Pt as described in Chapter 1 [64].

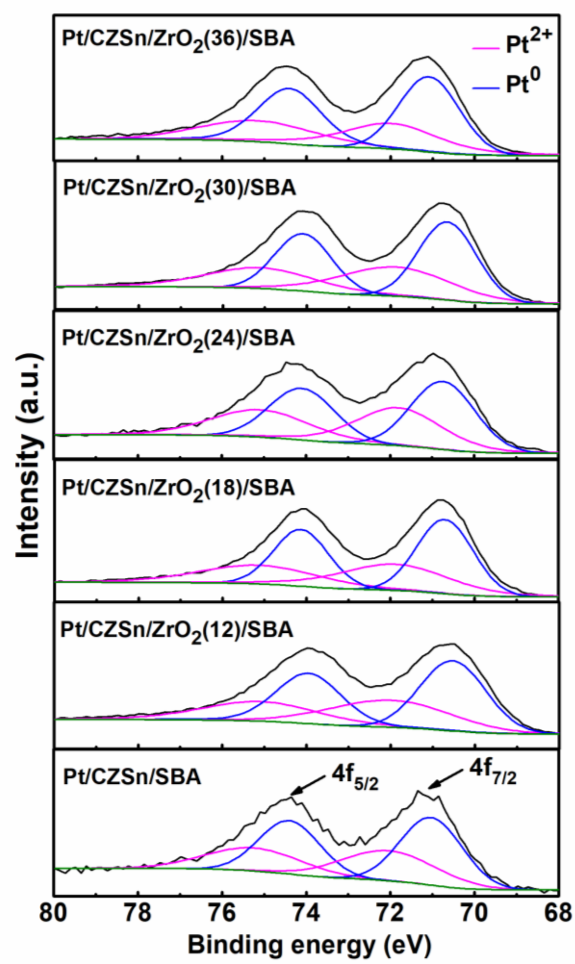

Figure 2.11. Deconvolution Pt 4f core level XPS spectra of the Pt/CZSn/ZrO_2(x)/SBA catalysts.

Table 2.3. Refinement parameter of deconvolution Pt 4f core level XPS spectra of the Pt/CZSn/ZrO_2(*x*)/SBA catalysts

Catalyst	Peak	Position (eV)	FWHM (eV)	Area (%)	$Pt^{2+}/(Pt^0+Pt^{2+})$ ratio (%)
Pt/CZSn/SBA (χ^2 = 0.0140)	Pt^{2+} $4f_{5/2}$	75.38	2.91	16.9	40
	Pt^0 $4f_{5/2}$	74.00	1.59	29.9	
	Pt^{2+} $4f_{7/2}$	72.00	1.98	19.7	
	Pt^0 $4f_{7/2}$	70.61	1.42	33.4	
Pt/CZSn/ZrO_2(12)/SBA (χ^2 = 0.0033)	Pt^{2+} $4f_{5/2}$	75.10	3.28	18.2	42
	Pt^0 $4f_{5/2}$	73.95	1.82	25.1	
	Pt^{2+} $4f_{7/2}$	72.00	3.37	23.7	
	Pt^0 $4f_{7/2}$	70.52	1.84	33.0	
Pt/CZSn/ZrO_2(18)/SBA (χ^2 = 0.0035)	Pt^{2+} $4f_{5/2}$	75.14	3.40	18.9	44
	Pt^0 $4f_{5/2}$	74.13	1.54	24.4	
	Pt^{2+} $4f_{7/2}$	71.90	3.06	24.6	
	Pt^0 $4f_{7/2}$	70.70	1.58	32.1	
Pt/CZSn/ZrO_2(24)/SBA (χ^2 = 0.0049)	Pt^{2+} $4f_{5/2}$	75.09	2.78	20.7	46
	Pt^0 $4f_{5/2}$	74.10	1.84	23.7	
	Pt^{2+} $4f_{7/2}$	71.80	2.4	25.0	
	Pt^0 $4f_{7/2}$	70.74	1.79	30.6	
Pt/CZSn/ZrO_2(30)/SBA (χ^2 = 0.0037)	Pt^{2+} $4f_{5/2}$	75.10	3.14	18.6	43
	Pt^0 $4f_{5/2}$	74.09	1.59	24.0	
	Pt^{2+} $4f_{7/2}$	71.90	3.13	24.6	
	Pt^0 $4f_{7/2}$	70.65	1.62	32.8	
Pt/CZSn/ZrO_2(36)/SBA (χ^2 = 0.0040)	Pt^{2+} $4f_{5/2}$	75.16	3.33	18.5	41
	Pt^0 $4f_{5/2}$	74.40	1.77	27.7	
	Pt^{2+} $4f_{7/2}$	72.00	2.69	21.5	
	Pt^0 $4f_{7/2}$	71.08	1.68	32.3	

For the Pt/CZSn/ZrO_2(x)/SBA catalysts, the liquid-phase oxidation of phenol was carried out. Figure 2.12(a) displays the phenol removal percentage after the reaction at 80°C under the atmospheric air pressure as a function of reaction time, together with the data of Pt/CZSn/SBA (Chapter 1). For all the catalysts, the phenol removal percentage increased with expanding the reaction time. To investigate clearly the effect of ZrO_2 loading on the catalytic activity, the apparent reaction rate constant (k) was calculated. Here, since almost the linear relation between $-\ln(C/C_0)$ and t was obtained (Figure 2.12(b)), the k value was estimated using the pseudo-first-order reaction model using following equation:

$$\frac{\mathrm{d}C}{\mathrm{d}t} = -k\,C \tag{2}$$

where C and t are the phenol concentration after the reaction and the reaction time, respectively. Figure 2.13 presents the k value as a function of ZrO_2 loading amount. With increasing x, the k value increased up to $x = 24$, regardless of the decrease of the surface area (Table 2.2). This enhancement of the catalytic activity is considered to be attributed to the high concentration of the acidic sites of the support that improves the oxygen release and storage abilities of the promoter due to its high dispersibility. The high catalytic activity might be also related to the high $Pt^{2+}/(Pt^0+Pt^{2+})$ ratio due to the high oxygen release and storage abilities of the promoter [64]. For the samples with $x > 24$, the k value decreased with increasing x, likely because of the low acidity, the low surface area, the low oxygen release and storage abilities, and the low $Pt^{2+}/(Pt^0+Pt^{2+})$ ratio compared to the $x = 24$ case.

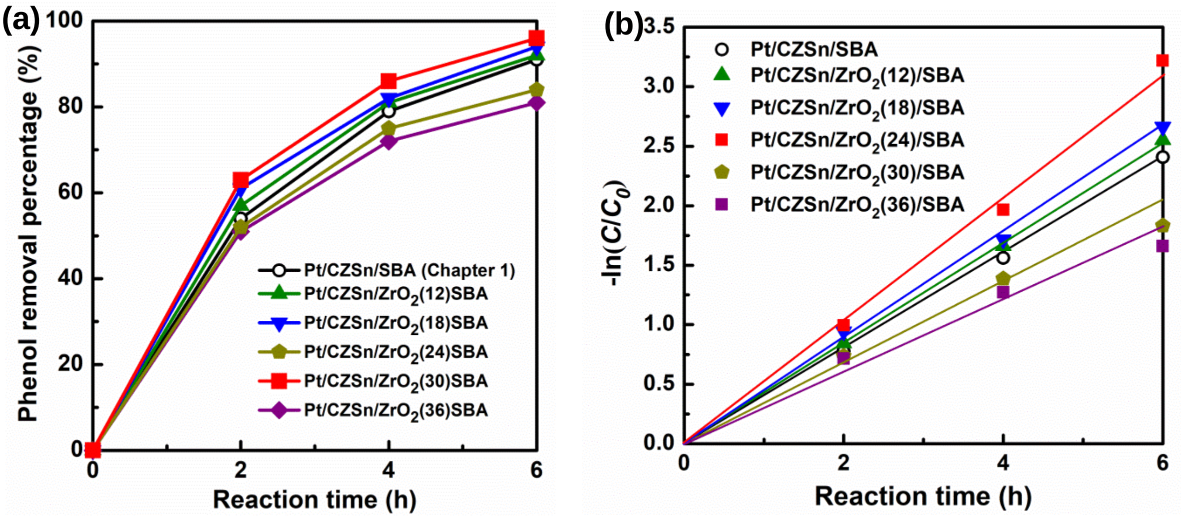

Figure 2.12. (a) Phenol removal percentages as a function of reaction time function and (b) plots of $-\ln(C/C_0)$ vs. reaction time for the Pt/CZSn/ZrO_2(*x*)/SBA catalysts.

(1000 ppm phenol 10 mL, 0.04 $g_{cat}\cdot mL^{-1}$, 80°C, atmospheric air pressure)

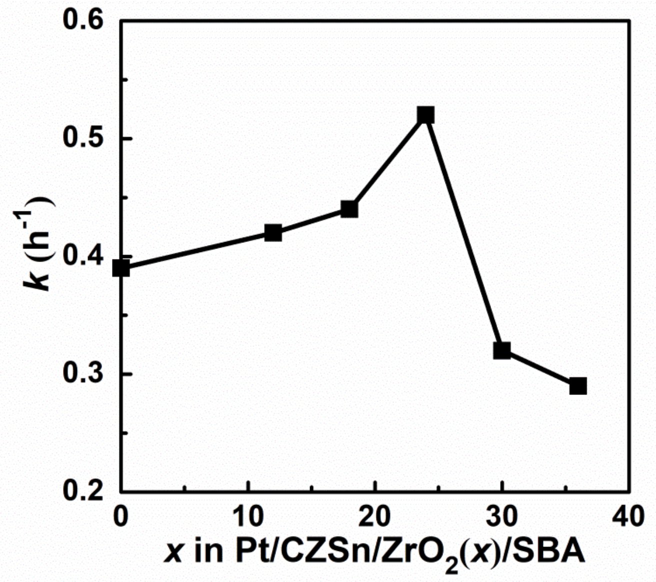

Figure 2.13. Relationship between the apparent reaction rate (*k*) values and the ZrO_2 loading amount (*x*).

Figure 2.14 depicts the catalytic phenol oxidation of the Pt/CZSn/ZrO_2(24)/SBA catalyst, which has the highest activity, with the data of Pt/CZSn/SBA described in Chapter 1. In the case of the Pt/CZSn/SBA catalyst that removed 91% of phenol after the reaction for 6 h, the complete phenol removal was still not achieved even after the reaction for 8 h (94%). By using Pt/CZSn/ZrO_2(24)/SBA, the phenol removal percentage reached up to 100% for 8 h; i.e., phenol was completely removed. Therefore, it was demonstrated that the ZrO_2(24)/SBA support increased the oxygen release and storage abilities of the CeO_2-ZrO_2-SnO_2 promoter, resulting in the highest catalytic activity of the Pt/CZSn/ZrO_2(24)/SBA catalyst. In addition, intermediate compounds such as acetic acid and benzoquinone were not detected for Pt/CZSn/ZrO_2(24)/SBA after the reaction for 8 h. Therefore, the phenol removal percentage after the reaction for 8 h (100%) was higher than the previous Pt/CZ catalyst (92%, 3 h, 160°C, 2.0 MPa of pure oxygen) [52].

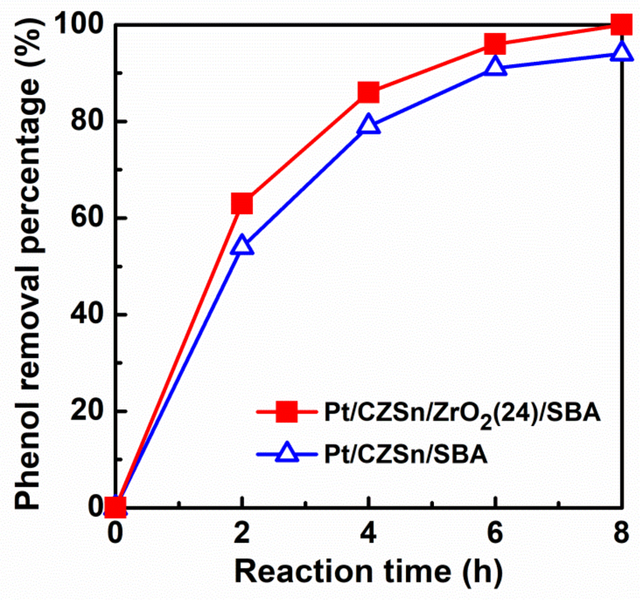

Figure 2.14. Phenol removal percentages as a function of reaction time function after the reaction using Pt/CZSn/ZrO_2(24)/SBA and Pt/CZSn/SBA catalysts.
(1000 ppm phenol 10 mL, 0.04 $g_{cat} \cdot mL^{-1}$, 80°C, atmospheric air pressure)

For Pt/CZSn/ZrO_2(24)/SBA, the reusability test was carried out for five cycles, and the results are shown in Figure 2.15. The catalytic activity maintained the high removal percentage above 97%; thus, Pt/CZSn/ZrO_2(24)/SBA has considerably high reusability.

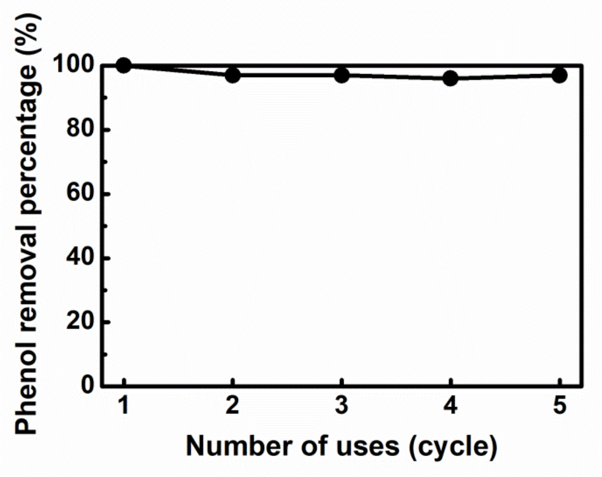

Figure 2.15. Reaction cycle dependence of the phenol removal percentage on the Pt/CZSn/ZrO_2(24)/SBA catalyst after the reaction for 8 h.
(1000 ppm phenol 10 mL, 0.04 $g_{cat}\cdot mL^{-1}$, 80°C, atmospheric air pressure)

2.4. Conclusion

In this chapter, for the complete removal of phenol, the catalytic activty was enhanced by the loading of ZrO_2 onto SBA-16 before supporting Pt and CeO_2-ZrO_2-SnO_2. The ZrO_2 loading increased the concentration of the acidic sites of the support, resulting in the improvement of the oxygen release and storage abilities of the promoter by prohibiting the aggregation of promoter. Among the prepared catalysts, the highest catalytic activity was obtained for the 7wt% Pt/ 16wt% $Ce_{0.68}Zr_{0.17}Sn_{0.15}O_2$/ 24wt% ZrO_2/SBA-16 catalyst, and as a result, the complete removal of phenol was successfully realized after the reaction for 8 h at 80°C under the atmospheric air pressure.

Chapter 3

Liquid-phase Oxidation of Phenol Using Pt/CeO_2-ZrO_2-Bi_2O_3 Supported on Size-controlled ZrO_2

3.1. Introduction

In Chapter 2, it was demonstrated that the ZrO_2 loading onto SBA-16 contributed to the high acidity and the large surface area, which enhanced the oxygen release and storage abilities resulting in the high catalytic activity, and the complete phenol removal was achieved for 7wt% Pt/ 16wt% $Ce_{0.68}Zr_{0.17}Sn_{0.15}O_2$/ 24wt% ZrO_2/SBA-16 after the reaction for 8 h at 80°C under the atmospheric air pressure. However, the detail relationship between the acidity of ZrO_2 and the catalytic activity still remains unclear; the knowledge of this relationship is highly important to develop the novel catalysts.

In order to investigate the effect of the acidity of ZrO_2 on the catalytic activity, size-controlled ZrO_2 nanoparticles with various particle sizes were used as the catalyst supports because the acidity is considered to be affected by the particle surface, that is, the size of ZrO_2. Here, to demonstrate the ZrO_2 particle size effect strictly, SBA-16 was excluded. In addition, it is necessary to maintain the particle size of the ZrO_2 nanoparticle during the catalyst preparation processes, especially at the calcination step at elevated temperatures. For the Pt/CeO_2-ZrO_2-SnO_2/SBA-16 system described in Chapter 1, while the Pt loading can be conducted at 500°C, the loading process of CeO_2-ZrO_2-SnO_2 requires at least 900°C to obtain the sufficient promoter property. Because such a high temperature should cause the aggregation and particle growth of

ZrO_2 nanoparticle, it is necessary to select another promoter with high oxygen release and storage abilities instead of CeO_2-ZrO_2-SnO_2. Here, the CeO_2-ZrO_2-Bi_2O_3 solid was focused as a candidate because the CeO_2-ZrO_2-Bi_2O_3 solid has been reported to exhibit the comparable oxygen release and storage abilities to the CeO_2-ZrO_2-SnO_2 solid [54]. Furthermore, since the CeO_2-ZrO_2-Bi_2O_3 solid can be loaded onto the support at as low as 600°C [70], CeO_2-ZrO_2-Bi_2O_3 is preferable to maintain the ZrO_2 nanoparticle size. Therefore, CeO_2-ZrO_2-Bi_2O_3 was selected as the promoter instead of CeO_2-ZrO_2-SnO_2.

Based on these concepts, Pt/CeO_2-ZrO_2-Bi_2O_3 loaded onto size-controlled ZrO_2 nanoparticles were prepared, and the relationship between the particle size of ZrO_2, the acidity, the oxygen release and storage abilities, and the catalytic activity for the phenol removal were investigated. As for the composition of CeO_2-ZrO_2-Bi_2O_3, I completely replaced the $Sn^{4+/2+}$ ion site in $Ce_{0.68}Zr_{0.17}Sn_{0.15}O_2$, mentioned in Chapter 1, by the Bi^{3+} ion; that is $Ce_{0.68}Zr_{0.17}Bi_{0.15}O_{2-\delta}$.

3.2. Experimental Procedure

Six types of size-controlled ZrO_2 nanoparticles (denoted as ZrO_2-*X* (*X*: A–F)), provided by Daiichi Kigenso Kagaku Kogyo, were used to investigate the ZrO_2 particle size effect on the catalytic activity. According to the transmission electron microscopy (TEM) images (H-800, Hitachi) as shown in Figure 3.1, the order of the particle-size was ZrO_2-A (40 nm) > ZrO_2-B (22 nm) > ZrO_2-C (14 nm) > ZrO_2-D (11 nm) > ZrO_2-E (9 nm) > ZrO_2-F (2 nm).

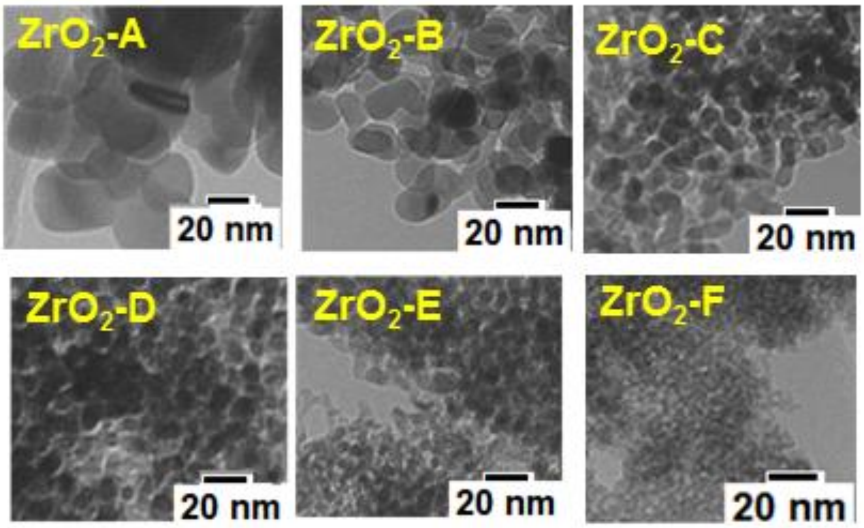

Figure 3.1. TEM images of the size-controlled ZrO_2-*X* (*X*: A-F) nanoparticles.

$Ce_{0.68}Zr_{0.17}Bi_{0.15}O_{2-\delta}$ loading onto ZrO_2-*X* was carried out via a wet impregnation procedure. The precursors of 1.0 mol·L^{-1} $Ce(NO_3)_3$ (0.75 mL), 0.1 mol·L^{-1} $ZrO(NO_3)_2$ (1.87 mL), and 0.5 mol·L^{-1} $Bi(NO_3)_3$ (0.33 mL) were mixed in water (40 mL), and then, the ZrO_2-*X* powder (1.0 g) was added. The mixture was stirred at room temperature for 6 h, followed by the evaporation of the solvent at 180°C and the calcination at 600°C for 1 h. Platinum loading was conducted via similar procedure described in Chapters 1 and 2. Here, the loading amounts of Pt and $Ce_{0.68}Zr_{0.17}Bi_{0.15}O_{2-\delta}$ were adjusted to be 7wt% and 16wt%, respectively, same as Chapter 1 in the Pt/CeO_2-ZrO_2-SnO_2/SBA series.

N_2 gas adsorption-desorption measurement was conducted, and the pore size distribution and the surface area were also assessed using the BJH and BET methods, respectively (Tristar 3000, Shimadzu). The samples were also characterized by using XRD measurement (SmartLab, Rigaku). Thermogravimetric-differential thermal analysis (TG-DTA) was conducted with the heating rate of 10°C·min^{-1} from room temperature to 600°C under the air flow (20 mL·min^{-1}) (DTA-60AH, Shimadzu). The concentration of the acidic sites was estimated from the NH_3-TPD profiles, where the sample was exposed to the flow of 0.5vol%NH_3-99.5vol%N_2 (50 mL·min^{-1}) at 50°C for 30 min, followed by the heating under a flow of He at the rate of 10°C·min^{-1} with monitoring the desorbed gas (BELCAT-B, MicrotracBEL). H_2-TPR measurement was carried out in 5vol%H_2-95vol%Ar flow (50 mL·min^{-1}) with the heating rate of 5°C·min^{-1}, followed by the OSC measurement using pulse injection method at 500°C (BELCAT-B, MicrotracBEL). X-ray photoelectron spectroscopy (XPS) analysis was performed to investigate the oxidation state of Pt at room temperature using Al-Kα radiation (PHI5000 Versa Probe II, ULVAC-PHI), and the spectra were fitted using Shirley background and Gaussian-Lorentzian line shape. The liquid-phase oxidation of phenol was carried out according to Chapter 1.

3.3. Results and Discussion

Figure 3.2 presents the N_2 adsorption-desorption isotherms and BJH pore size distributions of the ZrO_2-*X* (*X*: A–F) supports. According to the IUPAC classification, the isotherm curves of ZrO_2-*X* (*X*: A–F) (Figure 3.2(a)) have a type-II pattern which is typically non-porous materials [62]. The pore sizes estimated by the BJH pore size distribution (Figure 3.2(b)) are tabulated in Table 3.1, with the data of the particle sizes estimated from Figure 3.1. For each ZrO_2-*X* (*X*: A–F), the pore size was consistent with its particle size, suggesting that the pores were formed by the adjacent particles. Table 3.1 also shows the surface areas of the ZrO_2-*X* (*X*: A–F) supports. As expected, the surface area was inversely proportional to the particle size; that is, the surface area was increased with the decrease of particle size and ZrO_2-F exhibited the largest surface area among the supports.

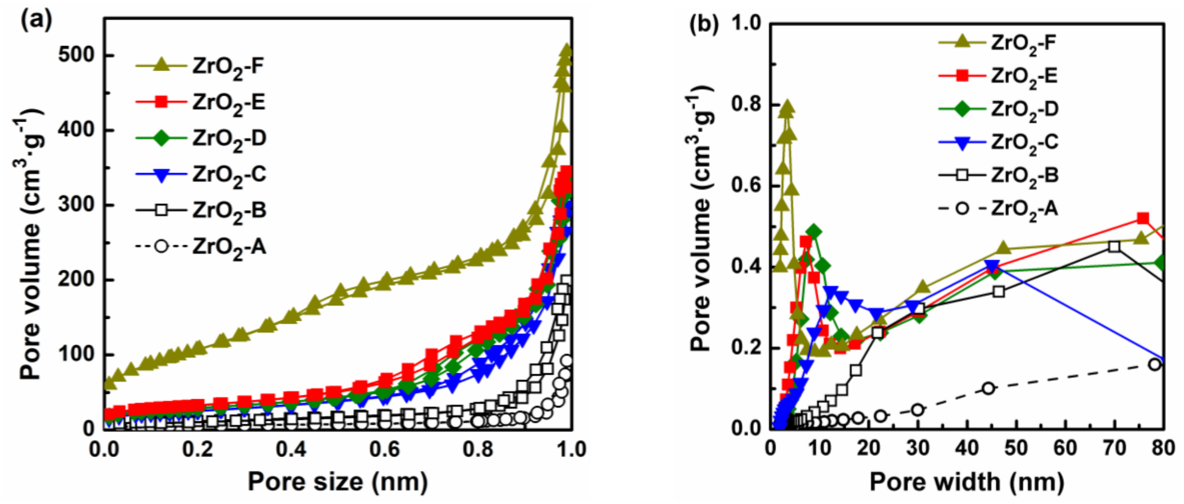

Figure 3.2. (a) N_2 adsorption-desorption isotherms and (b) BJH pore size distributions of the ZrO_2-*X* (*X*: A–F) supports.

Table 3.1. Particle size, pore size, and surface area of the ZrO_2-*X* (*X*: A–F) supports

Support	Particle size (nm)[a]	Pore size (nm)[b]	Surface area ($m^2 \cdot g^{-1}$)
ZrO_2-A	40	> 40	22
ZrO_2-B	22	21	51
ZrO_2-C	14	12	92
ZrO_2-D	11	9	129
ZrO_2-E	9	7	110
ZrO_2-F	2	3	390

[a]: Particle size estimated from the TEM images (Figure 3.1)
[b]: Pore size estimated from the BJH pore size distribution (Figure 3.2(b))

Figure 3.3 depicts the XRD patterns of the ZrO_2-*X* (*X*: A–F) supports. Diffraction peaks of the monoclinic ZrO_2 structure were clearly observed for ZrO_2-*X* (*X*: A–E), where a small amount of the tetragonal ZrO_2 phase was also observed in the case of ZrO_2-C, ZrO_2-D, and ZrO_2-E. On the other hand, ZrO_2-F has the amorphous phase, and TG-DTA result demonstrated that amorphous ZrO_2-F was crystallized at 430°C which is lower than the loading temperatures of CeO_2-ZrO_2-Bi_2O_3 (600°C) and Pt (500°C); therefore, ZrO_2-F was excluded from the candidate support material and the particle size effect was investigated by using the crystalline ZrO_2-*X* (*X*: A–E) supports.

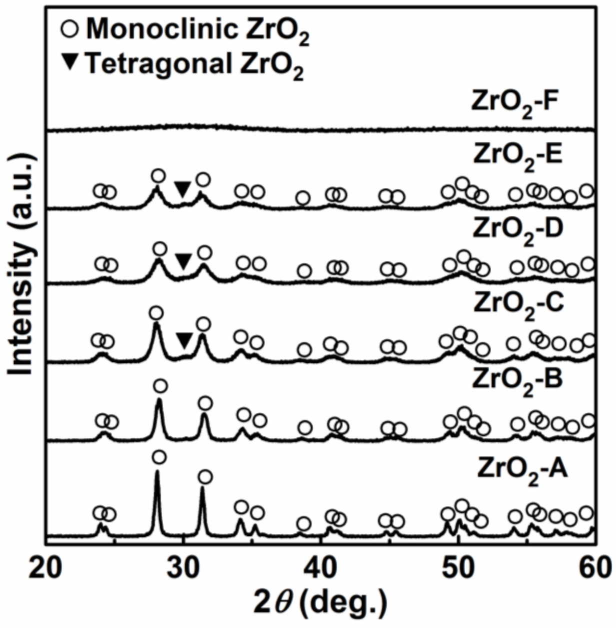

Figure 3.3. XRD patterns of the ZrO_2-*X* (*X*: A–F) supports.

Figure 3.4 shows the NH_3-TPD profiles of ZrO_2-*X* (*X*: A–E). For the ZrO_2-*X* (*X*: B–E) supports, three broad peaks were observed at temperature range of 100–200°C, 200–400°C, and > 400°C which are corresponding to the weak, intermediate, and strong acidic sites, respectively. On the other hand, the peak assignment for ZrO_2-A is difficult due to almost the constant and low-intensity from 100°C to 500°C. To investigate the effect of the particle size on the acidity of the ZrO_2 supports, the concentration of the acidic sites was calculated, and the results are shown in Figure 3.5. The concentration of the acidic sites was increased with the decrease of particle size, because the large surface area with the small particle size (Table 3.1) increased the number of the acidic sites derived from the surface Zr^{4+} ion in ZrO_2. The highest acidity was obtained for ZrO_2-E having the smallest particle size of 9 nm among the crystalline ZrO_2-*X* (*X*: A–E) supports.

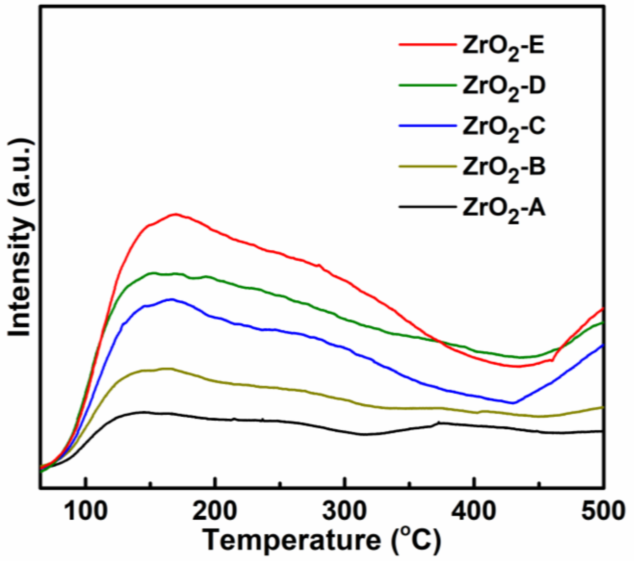

Figure 3.4. NH_3-TPD profiles of the ZrO_2-*X* (*X*: A–E) supports.

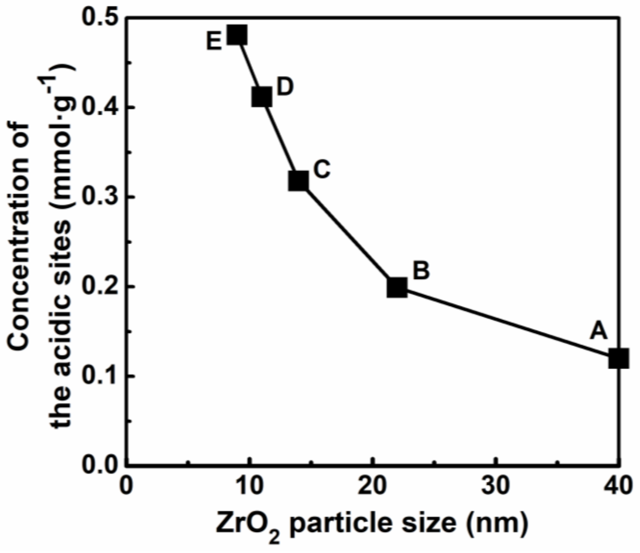

Figure 3.5. Effect of the ZrO_2 particle size on the concentration of the acidic sites in the ZrO_2-*X* (*X*: A–E) supports.

Figure 3.6 depicts the XRD patterns of the CZB/ZrO_2-*X* (*X*: A–E) samples. For all the samples, the monoclinic ZrO_2 phase was obviously observed. As for CZB/ZrO_2-E, while the monoclinic ZrO_2 was formed as the predominant phase, a small peak of the tetragonal phase was also observed at ca. 30 deg. Since it was revealed that the tetragonal phase was disappeared with the grain growth by the calcination of only ZrO_2-E at 600°C, this remaining tetragonal phase might be caused by maintaining the small particle size of ZrO_2 after the loading of CeO_2-ZrO_2-Bi_2O_3. For CZB/ZrO_2-*X* (*X*: A and B), the peak tailing (ca. 28 deg.) and low-intensity peak (ca. 47 deg.) were observed, assigned as the cubic fluorite-type structure of CeO_2-ZrO_2-Bi_2O_3, while these peaks could not be confirmed because of the overlapping of the broad peaks of monoclinic ZrO_2. Table 3.2 lists the surface area of CZB/ZrO_2-*X* (*X*: A–E). The introduction of CeO_2-ZrO_2-Bi_2O_3 decreased the surface area compared to the ZrO_2-*X* (*X*: A–E) support case (Table 3.1). In addition, the order of the surface areas of CZB/ZrO_2-*X* (*X*: A–E) has the same tendency as that of ZrO_2-*X* (*X*: A–E).

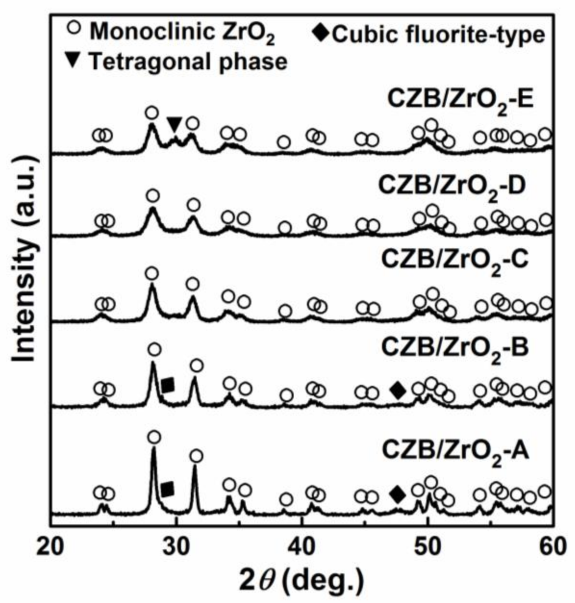

Figure 3.6. XRD patterns of the CZB/ZrO_2-*X* (*X*: A–E) samples.

Table 3.2. Surface area of the CZB/ZrO_2-*X* (*X*: A–E) samples

Sample	Surface area ($m^2 \cdot g^{-1}$)
CZB/ZrO_2-A	19
CZB/ZrO_2-B	40
CZB/ZrO_2-C	57
CZB/ZrO_2-D	65
CZB/ZrO_2-E	69

To investigate the effect of the ZrO_2 particle size on the oxygen release and storage abilities, the H_2-TPR and OSC measurements were carried out for CZB/ZrO_2-*X* (*X*: A–E). Figure 3.7 presents the H_2-TPR profiles of CZB/ZrO_2-*X* (*X*: A–E) with the fitting data. Two fitted peaks are attributed to the surface and bulk reductions of the CeO_2-ZrO_2-Bi_2O_3 promoter at lower and higher temperatures, respectively. The dependencies of the first reduction temperature in the TPR profile and the OSC value on the ZrO_2 particle size are shown in Figure 3.8. With decreasing the ZrO_2 particle size, the first reduction temperature decreased and the OSC value increased, indicating that the oxygen release and storage abilities improved. These improvements of the oxygen release and storage abilities might be attributed to the phenomenon that the high concentration of the acidic sites led to the high dispersion of the CeO_2-ZrO_2-Bi_2O_3 promoter, resulting in the increase of the number of the active sites for the oxygen release and storage [55,56]. The large surface area of the ZrO_2 support is also considered to affect the high dispersion of the CeO_2-ZrO_2-Bi_2O_3. Among the samples, the highest oxygen release and storage abilities were obtained for the CZB/ZrO_2-E sample, where ZrO_2-E has the highest acidity and the largest surface area owing to the smallest particle size of 9 nm among crystalline ZrO_2. Here, CZB/ZrO_2-E contained a small amount of tetragonal ZrO_2 (Figure 3.6) which is unfavorable for the reducibility of the loaded metal oxide compared to monoclinic ZrO_2 [71,72], indicating that the high acidity and the large surface area of ZrO_2 was considered to predominantly affect the enhancement of the reducibility.

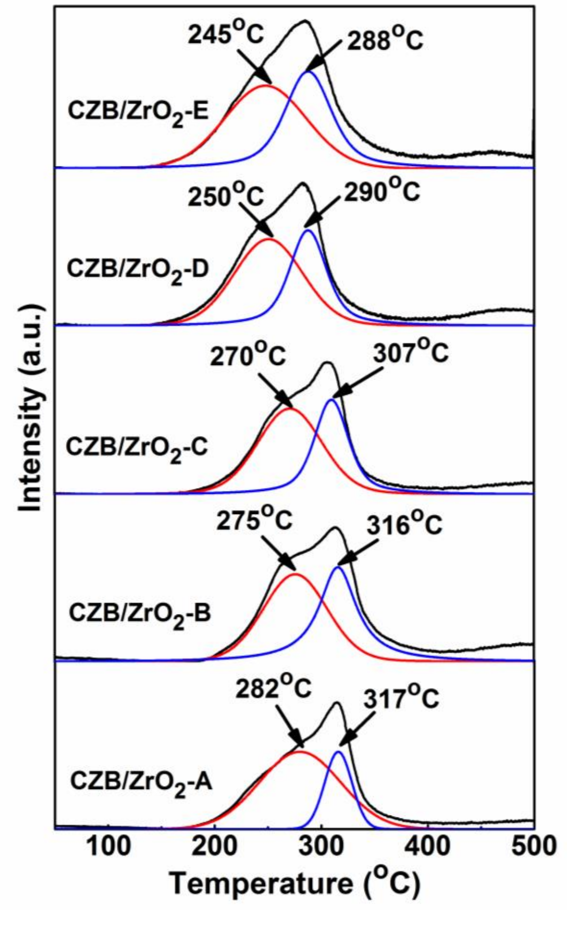

Figure 3.7. H_2-TPR profiles of the CZB/ZrO_2-*X* (*X*: A-E) samples.

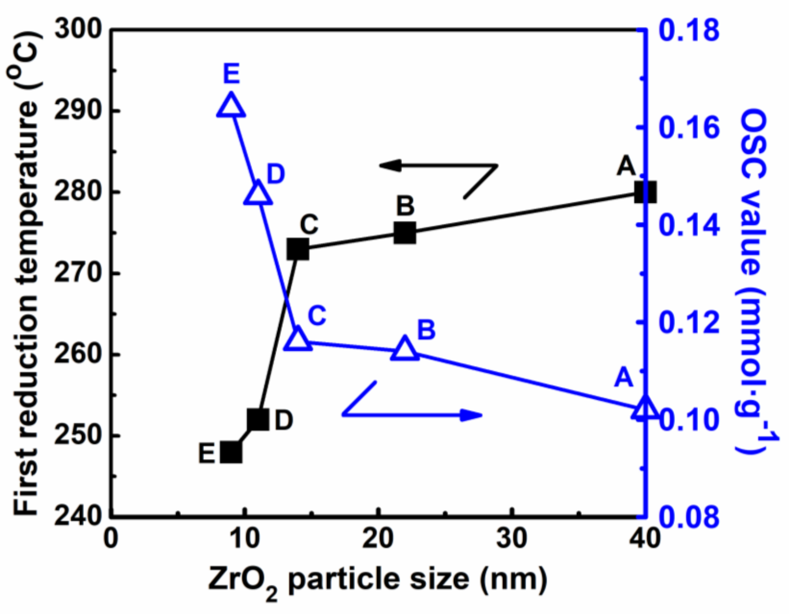

Figure 3.8. Dependencies of the reduction temperature and the OSC values on the ZrO_2 particle size for the CZB/ZrO_2-*X* (*X*: A–E) samples.

Figure 3.9 presents the XRD patterns of Pt/CZB/ZrO_2-*X* (*X*: A–E). The XRD patterns of Pt/CZB/ZrO_2-*X* (*X*: A–E) were similar to those of CZB/ZrO_2-*X* (*X*: A–E) (Figure 3.6), with the additional peaks attributed to the Pt metal. Figure 3.10 depicts the TEM images of the Pt/CZB/ZrO_2-*X* (*X*: A–E) catalysts. The ZrO_2 and Pt particles were clearly observed, while it is difficult to detect CeO_2-ZrO_2-Bi_2O_3 with low-crystallinity compared to ZrO_2 (Figure 3.6). Table 3.3 tabulates the ZrO_2 and Pt particle sizes, estimated from the TEM images. The ZrO_2 particle sizes after the loading of CeO_2-ZrO_2-Bi_2O_3 and Pt (Table 3.3) remained almost the same as the original sizes (Table 3.1). With decreasing the ZrO_2 particle size, the Pt particle size also decreased, indicating that the large surface area with the small ZrO_2 particle size caused the high dispersion of Pt. For the Pt/CZB/ZrO_2-*X* (*X*: A–E) catalysts, the surface area was measured, and the results are also tabulated in Table 3.3. By introducing Pt, the surface area of the catalysts slightly decreased compared to that of CZB/ZrO_2-*X* (*X*: A–E) (Table 3.2). Also, the surface area (Table 3.3) showed a trend similar to that of CZB/ZrO_2-*X* (Table 3.2).

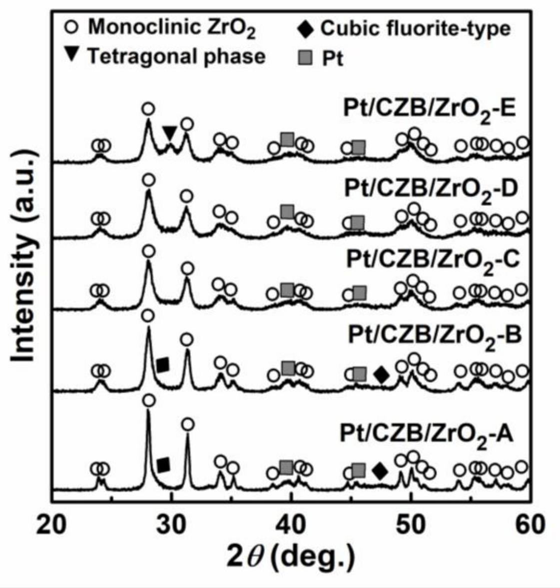

Figure 3.9. XRD patterns of the Pt/CZB/ZrO_2-*X* (*X*: A–E) catalysts.

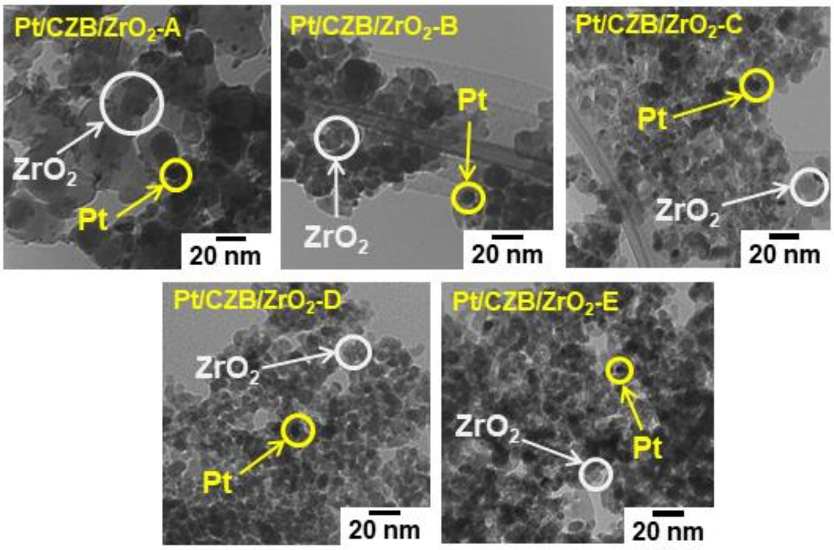

Figure 3.10. TEM images of the Pt/CZB/ZrO_2-*X* (*X*: A–E) catalysts.

Table 3.3. ZrO_2 and Pt particle sizes and surface area of the Pt/CZB/ZrO_2-*X* (*X*: A–E) catalysts

Catalyst	ZrO_2 particle size (nm)	Pt particle size (nm)	Surface area ($m^2 \cdot g^{-1}$)
Pt/CZB/ZrO_2-A	41	9.6	16
Pt/CZB/ZrO_2-B	22	8.8	38
Pt/CZB/ZrO_2-C	14	7.0	44
Pt/CZB/ZrO_2-D	11	6.3	59
Pt/CZB/ZrO_2-E	9	5.1	65

Figure 3.11 depicts the deconvoluted XPS spectra of Pt 4f core level of the Pt/CZB/ZrO_2-*X* catalysts, and the refinement parameters are tabulated in Table 3.4. The spectra revealed that both the $4f_{5/2}$ and $4f_{7/2}$ peaks can be assigned as Pt^{2+} and Pt^0. The $Pt^{2+}/(Pt^0+Pt^{2+})$ ratios of the catalysts, estimated from the XPS results are also listed in Table 3.4. The highest $Pt^{2+}/(Pt^0+Pt^{2+})$ ratio was obtained for Pt/CZB/ZrO_2-E followed by Pt/CZB/ZrO_2-D, Pt/CZB/ZrO_2-C, Pt/CZB/ZrO_2-B, and Pt/CZB/ZrO_2-A. Here, the generation of Pt^{2+} might be facilitated by the high oxygen release and storage abilities of the promoter [64], caused by the high concentration of the acidic sites. The large surface area might also increase dispersibility of Pt, resulting in the acceleration of oxidation of surface Pt [73,74].

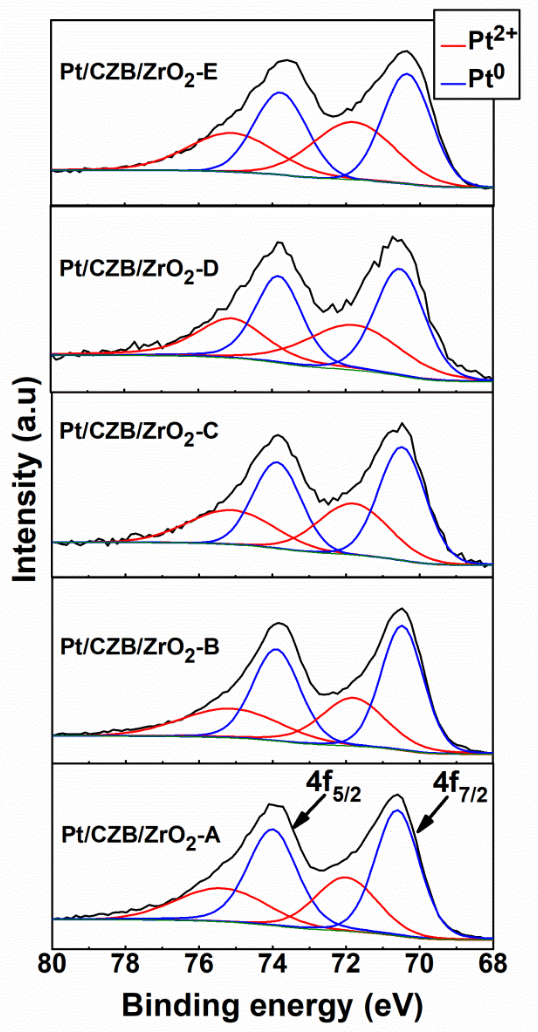

Figure 3.11. Deconvoluted XPS spectra of Pt 4f core level of the Pt/CZB/ZrO_2-*X* (*X*: A–E) catalysts.

Table 3.4. Refinement parameter of deconvolution Pt 4f core level XPS spectra of the Pt/CZB/ZrO_2-*X* (*X*: A–E) catalysts

Catalyst	Peak	Position (eV)	FWHM (eV)	Area (%)	$Pt^{2+}/(Pt^0+Pt^{2+})$ (%)
Pt/CZB/ZrO_2-A (χ^2 = 0.0087)	Pt^{2+} $4f_{5/2}$	75.38	2.91	16.92	36
	Pt^0 $4f_{5/2}$	74.00	1.59	29.93	
	Pt^{2+} $4f_{7/2}$	72.00	1.98	19.70	
	Pt^0 $4f_{7/2}$	70.61	1.42	33.44	
Pt/CZB/ZrO_2-B (χ^2 = 0.0065)	Pt^{2+} $4f_{5/2}$	75.13	3.20	17.46	38
	Pt^0 $4f_{5/2}$	73.90	1.52	27.87	
	Pt^{2+} $4f_{7/2}$	71.80	2.07	21.29	
	Pt^0 $4f_{7/2}$	70.47	1.36	33.38	
Pt/CZB/ZrO_2-C (χ^2 = 0.0085)	Pt^{2+} $4f_{5/2}$	75.11	2.77	18.15	42
	Pt^0 $4f_{5/2}$	73.87	1.54	25.42	
	Pt^{2+} $4f_{7/2}$	71.80	2.26	22.94	
	Pt^0 $4f_{7/2}$	70.47	1.49	33.49	
Pt/CZB/ZrO_2-D (χ^2 = 0.0110)	Pt^{2+} $4f_{5/2}$	75.10	2.25	19.24	44
	Pt^0 $4f_{5/2}$	73.82	1.50	24.87	
	Pt^{2+} $4f_{7/2}$	71.78	2.98	24.91	
	Pt^0 $4f_{7/2}$	70.53	1.58	30.98	
Pt/CZB/ZrO_2-E (χ^2 = 0.0077)	Pt^{2+} $4f_{5/2}$	75.10	2.80	20.00	46
	Pt^0 $4f_{5/2}$	73.78	1.68	24.09	
	Pt^{2+} $4f_{7/2}$	71.80	2.59	26.08	
	Pt^0 $4f_{7/2}$	70.35	1.55	29.83	

Figure 3.12 shows the phenol removal percentage as a function of reaction time using the Pt/CZB/ZrO_2-*X* (*X*: A–E) catalysts at 80°C under the atmospheric air pressure. The phenol removal percentage increased with increasing reaction time for all the catalysts. Among the prepared catalysts, the complete phenol removal was realized by using the Pt/CZB/ZrO_2-E catalysts after the reaction for 10 h, and it was confirmed that no intermediate compound was found by GCMS. To investigate the effect of the ZrO_2 particle size on the catalytic activity, the *k* value of each catalyst was estimated using the pseudo-first-order reaction model using the similar method as described in Chapter 2, because almost the linear relation between $-\ln(C/C_0)$ and *t* were obtained as shown in Figure 3.12(b). Figure 3.13 presents the relationship between the *k* value and the particle size of ZrO_2. The smaller particle size of the ZrO_2-*X* (*X*: A–E) support was, the higher *k* value of the Pt/CZB/ZrO_2-*X* (*X*: A–E) was. As a result, the highest catalytic activity was obtained for the Pt/CZB/ZrO_2-E catalyst with the smallest particle size of ZrO_2 (ZrO_2-E with 9 nm). This high catalytic activity was attributed to the high concentration of the acidic sites in addition to the large surface area, which improved the oxygen release and storage abilities. In addition, the high *k* value was also affected by the high Pt dispersion as well as the high $Pt^{2+}/(Pt^0+Pt^{2+})$ ratio caused by the high acidity and the large surface area.

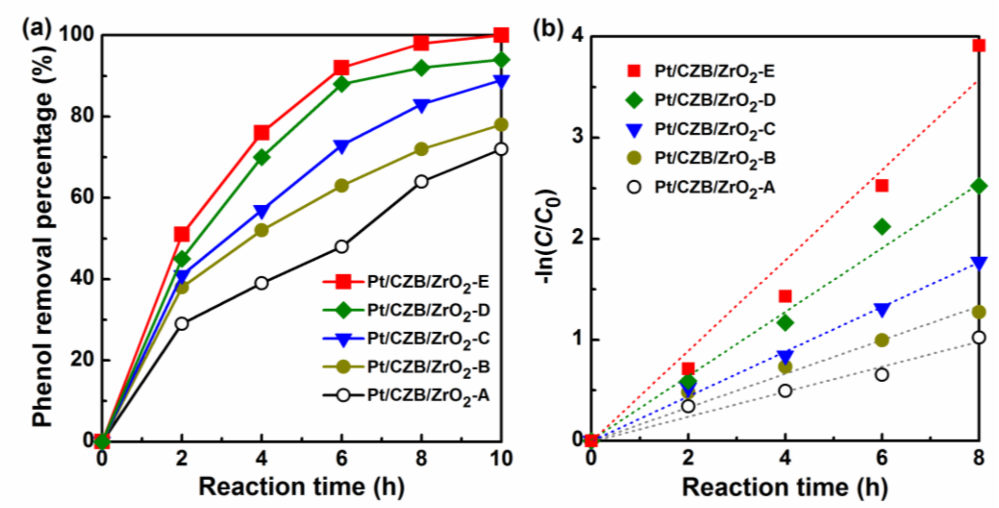

Figure 3.12. (a) Phenol removal percentages as a function of reaction time and (b) plots of $-\ln(C/C_0)$ vs. reaction time for the Pt/CZB/ZrO_2-*X* catalysts.
(1000 ppm phenol 10 mL, 0.04 $g_{cat}\cdot mL^{-1}$, 80°C, atmospheric air pressure)

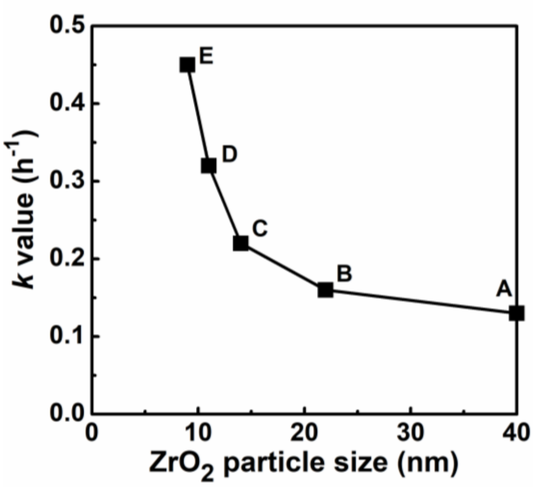

Figure 3.13. Relationship between the apparent reaction rate (*k*) values and the ZrO_2 particle size for Pt/CZB/ZrO_2-*X* (*X*: A–E).

3.4. Conclusion

In this chapter, to investigate the influence of the ZrO_2 particle size to the acidity, the oxygen release and storage abilities of the promoter, and the catalytic activity, the Pt/CeO_2-ZrO_2-Bi_2O_3 loaded on the size-controlled ZrO_2 nanoparticles were prepared. It was revealed that the smaller particle-size of the crystalline ZrO_2 support possessed the higher concentration of acidic sites as well as the large surface area, realizing the high catalytic activity with improving the oxygen release and storage abilities of the promoter.

Summary

In the work of this doctoral thesis, the catalysts with high activity have been developed for the effective decomposition of phenolic compounds in the liquid-phase under the moderate condition, i.e., at the temperatures below 100°C and under the atmospheric air pressure. The results obtained through this study are summarized as follows:

Chapter 1

For the effective decomposition of phenolic compounds under the moderate condition, the 7wt% Pt/ 16wt% $Ce_{0.68}Zr_{0.17}Sn_{0.15}O_2$/SBA-16 catalyst was proposed. This catalyst composed of the Pt activator, the CeO_2-ZrO_2-SnO_2 promoter with high oxygen release and storage abilities, and the SBA-16 support with high surface area. Since the CeO_2-ZrO_2-SnO_2 promoter effectively supplied the active oxygen species toward the Pt activator because of its improved oxygen release and storage abilities caused by the SnO_2 doping into the CeO_2-ZrO_2 lattice, the 7wt% Pt/ 16wt% $Ce_{0.68}Zr_{0.17}Sn_{0.15}O_2$/SBA-16 catalyst showed a 91% removal of phenol even at such a moderate condition of 6 h reaction time, at 80°C under the atmospheric air pressure. For the *p*-cresol oxidation, the present catalyst could remove the *p*-cresol completely after the reaction for 4 h at 80°C under the atmospheric air pressure. Because these reaction conditions were quite moderate compared to those for the previous catalysts, the superiority of the 7wt% Pt/ 16wt% $Ce_{0.68}Zr_{0.17}Sn_{0.15}O_2$/SBA-16 catalyst for the phenolic compound removal was successfully demonstrated.

Chapter 2

To realize the complete phenol removal by using the 7wt% Pt/ 16wt% $Ce_{0.68}Zr_{0.17}Sn_{0.15}O_2$/SBA-16 catalyst, ZrO_2 was additionally loaded onto the SBA-16 support. The ZrO_2 loading onto the SBA-16 realized the increase of the acidic sites of the support, resulting in the enhancement of the oxygen release and storage abilities of the promoter by suppressing the aggregation of promoter particles. The highest activity was obtained for the 7wt% Pt/ 16wt% $Ce_{0.68}Zr_{0.17}Sn_{0.15}O_2$/ 24wt% ZrO_2/SBA-16 catalyst, and the complete phenol removal was achieved after the reaction for 8 h at 80°C under the atmospheric air pressure.

Chapter 3

In order to clarify the effect of the acidity of the support, size-controlled ZrO_2 nanoparticles were applied as the support and the catalytic performances of the 7wt% Pt/ 16wt% $Ce_{0.68}Zr_{0.17}Bi_{0.15}O_{2-\delta}/ZrO_2$ were investigated. The acidity of crystalline ZrO_2 was increased with decreasing the ZrO_2 particle size, and as a result, the catalyst with smaller ZrO_2 was found to show the higher catalytic activity for phenol removal. Among the catalysts tested in this thesis, the highest activity was obtained for 7wt% Pt/ 16wt% $Ce_{0.68}Zr_{0.17}Bi_{0.15}O_{2-\delta}/ZrO_2$ using the ZrO_2 support with the smallest particle size of 9 nm.

References

[1] C.D. Silva, J. Gómez, R. Beristain-Cardoso, *Bioresour. Technol.*, 2011, **102**, 6464–6468.

[2] C. Ayral, C.J. Lebigue, F. Stüber, A.M. Wilhelm, H. Delmas, *Ind. Eng. Chem. Res.*, 2010, **49(21)**, 10707–10714.

[3] U.S. Kulkarni, S.G. Dixit, *Ind. Eng. Chem. Res.*, 1991, **30**, 1916–1920.

[4] S. Yang, W. Zhu, J. Wang, Z. Chen, *J. Hazard. Mater.*, 2008, **153**, 1248–1253.

[5] V.M. Brown, D.H.M. Jordan, B.A. Tiller, *Water Res.*, 1967, **1(8-9)**, 587–594.

[6] M.S. Roberts, R.A. Anderson, *J. Pharm. Pharmacol.*, 1975, **27**, 599–605.

[7] M.S. Roberts, R.A. Anderson, J. Swarbrick, *J. Pharm. Pharmacol.*, 1977, **29**, 677–683.

[8] N. Schweigert, A.J. Zehnder, R.I. Eggen, *Environ. Microbiol.*, 2001, **3**, 81–91.

[9] L.G.C. Villegas, N. Mashhadi, M. Chen, D. Mukherjee, K.E. Taylor, N. Biswas, *Curr. Pollut. Rep.*, 2016, **2**, 157–167.

[10] W.W. Anku, M.A. Mamo, P.P. Govender, *Phenolic Compounds - Natural Sources, Importance and Applications: Chapter 17*, 2017, 419–444. Intechopen, http://dx.doi.org/10.5772/66927

[11] G.S. dos Reis, M.A. Adebayo, C.H. Sampaio, E.C. Lima, P.S. Thue, I.A.S. de Brum, S.L.P. Dias, F.A. Pavan, *Water Air Soil Pollut.*, 2017, **228(33)**, 1–17.

[12] Y. Zhu, P. Kolar, *J. Environ. Chem. Eng.*, 2014, **2**, 2050–2058.

[13] S. Jiménez, M.M. Micó, M. Arnaldos, E. Ferrero, J.J. Malfeito, F. Medina, S. Contreras, *Chemosphere*, 2017, **168**, 309–317.

[14] M. Achak, F. Elayadi, W. Boumya, *Am. J. Appl. Sci.*, 2019, **16**, 59–91.

[15] T.P. Chung, H.Y, Tseng, R.S. Juang, *Process Biochem.*, 2003, **38(10)**, 1497–1507.

[16] R.K. Singh, S. Kumar, S. Kumar, A. Kumar, *Biochem. Eng. J.*, 2008, **40**, 293–303.

[17] L.H. Gracioso, P.B. Vieira, M.P.G. Baltazar, I.R. Avanzi, B. Karolski, C.A.O. Nascimento, E.A. Perpetuo, *Water Environ. J.*, 2019, **33**, 40–50.

[18] M.D. Gurol, R. Vatistas, *Water Res.*, 1987, **21(8)**, 895–900.

[19] Y. Zheng, D.O. Hill, C.H. Kuo, *J. Hazard. Mater.*, 1993, **34**, 245–260.

[20] S. Muhammad, E. Saputra, H. Sun, H.M. Ang, M.O. Tade, S. Wang, *Ind. Eng. Chem. Res.*, 2012, **51**, 15351–15359.

[21] S.G. Poulopoulos, F. Arvanitakis, C.J. Philippopoulos, *J. Hazard. Mater.*, 2006, **129(1-3)**, 64–68.

[18] H. Zhao, Y. Dong, G. Wang, P. Jiang, J. Zhang, L. Wu, K. Li, *Chem. Eng. J.*, 2013, **219**, 295–302.

[19] P. Shukla, S. Wang, K. Singh, H.M. Ang, M.O. Tadé, *Appl. Catal. B: Environ.*, 2010, **99(1-2)**, 163–169.

[20] H. Sun, C.K. Kwan, A. Suvorova, H.M. Ang, M.O. Tadé, S. Wang, *Appl. Catal. B: Environ.*, 2014, **154–155**, 134–141.

[21] P. Kumar, H. Nikakhtari, M. Nemati, G.A. Hill, *Environ. Technol.*, 2010, **31**, 47–52.

[22] C. Valdés, J. Alzate-Morales, J. Villaseñor, C. Navarro-Retamal, *Chem. Phys. Lett.*, 2015, **640**, 16–22.

[23] S.S. Sablea, K.J. Shaha, P.C. Chianga, S.L. Lo, *J. Taiwan Inst. Chem. E.*, 2018, **91**, 434–440.

[24] H. El-Hamshary, M.H. El-Newehy, S.S. Al-Deyab, *Molecules*, 2011, **16**, 9900–9911.

[25] H. Lee, J. Seong, K.M. Lee, H.H. Kim, J. Choi, J.H. Kim, C. Lee, *J. Hazard. Mater.*, 2018, **344**, 1174–1180.

[26] Y. Wang, H. Sun, H.M. Ang, M.O. Tadé, S. Wang, *ACS Appl. Mater. Interfaces*, 2014, **6**, 19914−19923.

[27] C.R. Huang, H.Y, Shuj, *J. Hazard. Mater.*, 1995, **41**, 47–64.

[28] A. Babuponnusami, K. Muthukumar, *Chem. Eng. J.*, 2012, **183**, 1–9.

[29] H. Liu, M.Y. Liang, C.S. Liu, Y.X. Gao, J.M. Zhou, *Chem. Eng. J.*, 2009, **153**, 131–137.

[30] V.S. Mishra, V.V. Mahajani, J.B. Joshi, *Ind. Eng. Chem. Res.*, 1995, **34(1)**, 2–48.

[31] M.E. Suárez-Ojeda, J. Carrera, I.S. Metcalfe, J. Font, *Chem. Eng. J.*, 2008, **144**, 205–212.

[32] S.H. Lin, T.S. Chuang, *Toxicol. Environ. Chem.*, 1994, **44(3-4)**, 243–258.

[37] Z.P.G. Masende, B.F.M. Kuster, K.J. Ptasinski, F.J.J.G. Janssen, J.H.Y. Katima, J.C. Schouten, *Catal. Today*, 2003, **79–80**, 357–370.

[33] R.R. Zapico, P. Marín, F.V. Díez, S. Ordóñez, *Chem. Eng. J.*, 2015, **270**, 122–132.

[34] J. Vicente, R. Rosal, M. Díaz, *J. Chem. Technol. Biotechnol.*, 2005, **80**, 1031–1035.

[35] H. Chen, A. Sayari, A. Adnot, F. Larachi, *Appl. Catal. B: Environ.*, 2001, **32**, 195–204.

[36] S.K. Kim, S.K. Ihm, *Top. Catal.*, 2005, **33**, 171–179.

[37] S.K. Kim, K.H. Kim, S.K. Ihm, *Chemosphere*, 2007, **68**, 287–292.

[38] K.H. Kim, J.R. Kim, S.K. Ihm, *J. Hazard. Mater.*, 2009, **167**, 1158–1162.

[39] Q. Wu, X. Hu, P.L. Yue, X.S. Zhao, G.Q. Lu, *Appl. Catal. B: Environ.*, 2001, **32**, 151–156.

[40] I.P. Chen, S.S. Lin, C.H. Wang, S.H. Chang, *Chemosphere*, 2007, **66**, 172–178.

[41] I.P. Chen, S.S. Lin, C.H. Wang, L. Chang, J.S. Chang, *Appl. Catal. B: Environ.*, 2004, **50**, 49–58.

[42] S. Hočevar, U.O. Krašovec, B. Orel, A.S. Aricó, H. Kim, *Appl. Catal. B: Environ.*, 2000, **28**, 113–125.

[43] F. Arena, R. Giovenco, T. Torre, A. Venuto, A. Parmaliana, *Appl. Catal. B: Environ.*, 2003, **45**, 51–62.

[44] E. Castillejos-López, A. Maroto-Valiente, D.M. Nevskaia, V. Muñoz, I. Rodríguez-Ramos, A. Guerrero-Ruiz, *Catal. Today*, 2009, **143**, 355–363.

[45] J. Barbier, L. Oliviero, B. Renard, D. Duprez, *Top. Catal.*, 2005, **33**, 77–86.

[46] A.E. de los Monteros, G. Lafaye, A. Cervantes, G.D. Angel, J. Barbier Jr., G. Torres, *Catal. Today*, 2015, **258**, 564–569.

[47] Z.P.G. Masende, B.F.M. Kuster, K.J. Ptasinski, F.J.J.G. Janssen, J.H.Y. Katim, J.C. Schouten, *Top. Catal.*, 2005, **33**, 87–99.

[48] S.K Kim, S.K. Ihm, *Ind. Eng. Chem. Res.*, 2002, **41**, 1967–1972.

[49] S. Bedrane, C. Descorme, D. Duprez, *Catal. Today*, 2002, **75**, 401–405.

[50] M. Ozawa, T. Okouchi, M. Haneda, *Catal. Today*, 2015, **242**, 329–337.

[51] P. Fornasiero, R. Dimonte, G.R. Rao, J. Kaspar, S. Meriani, A. Trovarelli, M. Graziani, *J. Catal.*, 1995, **151**, 168–177.

[52] S. Nousir, S. Keav, J. Barbier Jr., M. Bensitel, R. Brahmi, D. Duprez, *Appl. Catal. B: Environ.*, 2008, **84**, 723–731.

[53] S. Keav, A. Martin, J. Barbier Jr., D. Duprez, *Catal. Today*, 2010, **151**, 143–147.

[54] K. Yasuda, A. Yoshimura, A. Katsuma, T. Masui, N. Imanaka, *Bull. Chem. Soc. Jpn.*, 2012, **85**, 522–526.

[55] X. Gao, J.L.G. Fierro, I.E. Wachs, *Langmuir*, 1999, **15**, 3169–3178.

[56] S. Garg, K. Soni, G.M. Kumaran, M. Kumar, J.K. Gupta, L.D. Sharma, G.M. Dhar, *Catal. Today*, 2008, **130**, 302–308.

[57] H. Yotou, T. Okamoto, M. Ito, T. Sekino, S.-I. Tanaka, *Appl. Catal. A: Gen.* 2013, **458**, 137–144.

[58] D. Zhao, Q. Huo, J. Feng, B.F. Chmelka, G.D. Stucky, *J. Am. Chem. Soc.*, 1998, **120(24)**, 6024–6036.

[59] P.G. Choi, N. Nunotani, N. Imanaka, *Int. J. Appl. Ceram. Technol.*, 2017, **14**, 9–15.

[60] D.C. Thompson, K. Perera, R. Fisher, K. Brendel. *Toxicol. Appl. Pharmacol.*, 1994, **125**, 51–58.

[61] F. Izumi, K. Momma, *Solid State Phenom.*, 2007, **130**, 15–20.

[62] K.S.W. Sing, D.H. Evereet, R.A.W. Haul, L. Moscou, R. Pierotti, J. Rouquerol, T. Siemieniewska, *Pure Appl. Chem.*, 1985, **57(4)**, 603–619.

[63] R.D. Shannon, *Acta Crystallogr.*, 1976, **A32**, 751–767.

[64] M.A.L. Rocha, G.D. Ángel, G. Torres-Torres, A. Cervantes, A. Vázquez, A. Arrieta, J.N. Beltramini, *Catal. Today*, 2015, **250**, 145–154.

[65] F. Núñez, G.D. Angel, F. Tzompantzi, J. Navarrete, *Ind. Eng. Chem. Res.*, 2011, **50**, 2495–2500.

[66] S. Mu, D. Li, B. Hou, L. Jia, J. Chen, Y. Sun, *Energ. Fuel*, 2010, **24**, 3715–3718.

[67] C.K. Krishnan, T. Hayashi, M. Ogura, *Adv. Mater.*, 2008, **20**, 2131–2136.

[68] S.S. Enumula, V.R. Babu Gurram, M. Kondeboina, D.R. Burri, S.R.R. Kamaraju, *RSC Adv.*, 2016, **6**, 20230–20239.

[69] T. Hirata, E. Asari, M. Kitajima, *J. Solid State Chem.*, 1994, **110**, 201–207.

[70] P.G. Choi, T. Ohno, N. Fukuhara, T. Masui, N. Imanaka, *J. Adv. Ceram.*, 2015, **4**, 71–75.

[71] A.G. Sato, D.P. Volanti, D.M. Meira, S. Damyanova, E. Longo, J.M.C. Bueno, *J. Catal.*, 2013, **307**, 1–17.

[72] W. Li, H. Huang, H. Li, W. Zhang, H. Liu, *Langmuir*, 2008, **24**, 8358–8366.

[73] S. Gatla, D. Aubert, V. Flaud, R. Grosjean, T. Lunkenbein, O. Mathon, S. Pascarelli, H. Kaper, *Catal. Today*, 2019, **333**, 105–112.

[74] N. An, X. Yuan, B. Pan, Q. Li, S. Li, W. Zhang, *RSC Adv.*, 2014, **4**, 38250–38257.

Acknowledgments

The author would like to express his heartfelt gratitude to Professor Dr. Nobuhito Imanaka, Department of Applied Chemistry, Graduate School of Engineering, Osaka University, for his continuous guidance, many invaluable suggestions, and science encouragement throughout the work. The author is very grateful to Dr. Naoyoshi Nunotani, Department of Applied Chemistry, Graduate School of Engineering, Osaka University, for his continuous guidance and stimulating discussions for carrying out this work. The author is also indebted to Dr. Shinji Tamura, Department of Applied Chemistry, Graduate School of Engineering, Osaka University, for his helpful suggestions and apposite advice.

The author is deeply grateful to Professor Dr. Hiroshi Uyama, Department of Applied Chemistry, Graduate School of Engineering, Osaka University, and Professor Dr. Takahiro Kozawa, the Institute of Scientific and Industrial Research (Department of Applied Chemistry, Graduate School of Engineering), Osaka University, for reviewing this thesis and giving their valuable comments.

The Monbukagakusho/ MEXT Scholarship, Japan is also acknowledged for financial support during the author's study.

I wish to thank Dr. Hirokazu Izumi (Hyogo Prefectural Institute of Technology) for their help with the XPS measurements. I also thank Dr. Takao Sakata and Professor Dr. Hidehiro Yasuda (Research Center for Ultra-High Voltage Electron Microscopy, Osaka University) for assisting with the TEM observations.

Special thanks should be given to author's co-workers, Mr. Kenji Matsuo, Dr. Pil-Gyu Choi, Dr. Chang-Min Cho, Dr. Minchan Jeong, Mr. Naoki Moriyama, Mr. Muhammad Radzi Iqbal Bin Misran, Mr. Hiroaki Shirai, Mr. Masanari Takashima, Ms. Marina Taira, Mr. Yeon-Bin Choi, Mr. Yang Li, Ms. Li Zhouwei, Mr. Kenjiro Kakihana for their helpful assistance and support in the course of this work, and the other members of the research group under direction of Professor Dr. Nobuhito Imanaka, Osaka University.

The author would like to thank to Professor Dr. Djulia Onggo of Bandung Institute of Technology in Indonesia for her helpful encouragement. Finally, the author would like to extend deep gratitude to his parents, Mr. Gebog and Ms. Onyih, his parents-in-law Mr. Dodo and Ms. Yeti, his wife Ms. Eka Sulistiawati, his two sons Muhammad Atharrazka Gibran Rafizqy and Muhammad Askar Ryuzaki, and all the member of his family for their encouragement, continuous understanding, and perpetual supports.